Science Advances
AAAS

Title: The nuclear piston activates mechanosensitive ion channels to generate cell migration paths in confining microenvironments

Authors: Hong-pyo Lee[1], Farid Alisafaei[2], Kolade Adebawale[3], Julie Chang[4], Vivek B. Shenoy[2], Ovijit Chaudhuri[1*]

Affiliations:

[1]Department of Mechanical Engineering, Stanford University, CA, USA.

[2]Department of Bioengineering, University of Pennsylvania, Philadelphia, PA, USA

[3]Department of Chemical Engineering, Stanford University, CA, USA

[4]Department of Bioengineering, Stanford University, CA, USA

*Correspondence to: chaudhuri@stanford.edu.

Abstract :

Cell migration in confining microenvironments is limited by the ability of the stiff nucleus to deform through pores when migration paths are pre-existing and elastic, but how cells generate such paths remains unclear. Here, we reveal a mechanism by which the nucleus mechanically generates migration paths for mesenchymal stem cells (MSCs) in confining microenvironments. MSCs migrate robustly in nanoporous, confining hydrogels that are viscoelastic and plastic, but not in hydrogels that are more elastic. In order to migrate, MSCs first extend thin protrusions that widen over time due to a nuclear piston, thus opening up a migration path in the confining matrix. Theoretical modeling and experiments indicate that the nucleus pushing into the protrusion activates mechanosensitive ion channels, leading to an influx of ions that increases osmotic pressure, which outcompetes hydrostatic pressure to drive protrusion expansion. Thus, instead of limiting migration, the nucleus powers migration by generating migration paths.

One Sentence Summary :
The nuclear piston activates mechanosensitive ion channels to expand protrusions and generate migration paths in confining matrices.

MAIN TEXT

Introduction

Cell migration in 3D microenvironments plays a critical role in development, immune cell trafficking, tissue regeneration, and metastasis. During healing of bone fractures, MSC migration to the fracture sites through 3D microenvironments is critical for bone regeneration(Fig. 1A) (*1*, *2*). MSC migration is also essential for stem cell therapies involving the delivery of MSCs in biomaterial carriers(*3*, *4*). Interestingly, the 3D microenvironments in which MSCs migrate *in vivo*, including bone marrow and fracture hematomas, are

confining and are viscoelastic, exhibiting time dependent mechanical responses such as stress relaxation in response to deformation (*5*, *6*). Although many studies have examined the impact of matrix viscoelasticity on MSC spreading and differentiation(*5*, *7–11*), little is known about the physical process of how MSCs generate migration paths and migrate in confining and viscoelastic matrices.

The nucleus plays a complex role in 3D cell migration in confining matrices. The widely-held view is that the stiff nucleus limits the ability of cells to squeeze through nanometer-scale pores in confining extracellular matrix (ECM)(*12*, *13*). However, a set of studies showed that the nucleus can act as piston to generate increased hydrostatic pressure in lobopodial protrusions in fibroblasts and protease-inhibited tumor cells in reconstituted collagen gels (*14*, *15*). The piston was found to mediate lobopodial 3D migration, though the mechanism remains unclear, as the increase in hydrostatic pressure in the protrusion would be expected to drive water out of the protrusion. Further, a recent study revealed that the nucleus acts as a mechanical gauge in identifying the microchannel of least resistance in immune cells (*16*). Importantly, most studies of confined cell migration involve contexts in which migration paths or holes are pre-existing and elastic, or in which cells use proteases to degrade a migration path (*17–25*). While mechanisms by which cells utilize proteases to generate migration paths for nuclear translocation in ECM are now well understood(*20*, *26*, *27*), the use of protease-independent mechanisms in generating migration paths are largely unclear, and the functional role of the nuclear piston in cell migration is unknown. Only recently was it found that cancer cells can use mechanical force to open up a migration path in confining ECM only when the ECM exhibited sufficient mechanical plasticity, but the role of the nucleus was not described (*28*). Here, we reveal a previously undescribed role of the nucleus in migration, in which MSCs use a nuclear piston to open up a migration path through confining viscoelastic microenvironments.

Results

MSCs migrate in viscoelastic and plastic matrices by mechanically generating a migration path

Here we examine MSC migration in 3D in engineered alginate hydrogels, used as models of a fracture hematoma and biomaterial-based stem cell delivery carriers. Alginate hydrogels are nanoporous and cannot be degraded by mammalian enzymes, serving as a model confining microenvironment and facilitating discovery of protease-independent mechanisms of migration(*5*, *29*). While alginate itself is inert to cell adhesion, RGD was coupled to the alginate to promote integrin-mediated cell adhesion to the gels. Alginate hydrogel viscoelasticity and mechanical plasticity, as respectively assessed by stress relaxation tests and creep-recovery tests, can be modulated independent of degradability, pore size, and initial modulus by varying alginate molecular weight and crosslinking density(*5*, *28*, *30*). Alginate hydrogels formed low molecular weight alginate showed fast stress relaxation ($\tau_{1/2}$, or the time for stress to be relaxed to half its original value in shear, was ~80s), similar to that of a fracture hematoma, and were mechanically plastic (Permanent deformation of ~30 % in a 1h creep/1.7h recovery test, also in shear), while those formed from high molecular weight alginate were more elastic, exhibiting slow stress relaxation ($\tau_{1/2}$ was ~19,000s) and lower mechanical plasticity (Permanent deformation, ~25%) (*5*, *31*) (Fig. 1B-C, fig. S1A-D). Crosslinking density was tuned so that both exhibited similar initial elastic moduli of ~19kPa, previously reported as the optimal modulus to promote osteogenesis (*5*, *32*) (fig. S1E). Thus, the alginate hydrogels provide a confining microenvironment with independently tunable viscoelasticity/plasticity and ligand density for 3D culture.

Next, 3D migration of MSCs in the hydrogels was studied. To visualize MSC migration in the hydrogels, MSCs were stained with a membrane dye prior to encapsulation in the hydrogels, and then time-lapse confocal fluorescence microscopy was performed. Strikingly, MSCs were able to migrate in fast relaxing and plastic hydrogels, while MSCs maintained rounded cell morphology and did not migrate in the more elastic hydrogels (Fig. 1E, Movie S1 and 2). Cell tracking analysis indicates that cells in fast relaxing and plastic hydrogels migrate with greater speed and persistence than those in the more elastic hydrogels (Fig.

1F-H). Together these data establish that matrix viscoelasticity and plasticity are critical for migration of MSCs in 3D matrices that are confining and not susceptible to degradation by proteases.

We next investigated the mechanism by which the MSCs build the migration paths to migrate in the confining gels that were fast relaxing and exhibited mechanical plasticity. MSCs initially extend long shallow protrusions into the fast relaxing and plastic hydrogels, which then widened over time, eventually allowing migration to occur (Fig. 2A, B). This widening process was accompanied by volume expansion in the protrusion (fig. S2A, B). More protrusive cells, as indicated by a lower sphericity, exhibited larger volumes than rounded cells (fig. S2C). When body and protrusion volume were separately analyzed, the body volume was found to be similar before and after protrusion expansion, while the protrusion volume increased significantly (Fig. 2C, D). These data indicate that total volume of single cell increases due to volume expansion in the protrusion and not the body. The 3D volume measurements were conducted by reconstructing 3D cell volume from a 2D stack of confocal microscope images; we previously confirmed that the volumes measured using this method matches that measured using super-resolution microscopy (*10*). Since alginate hydrogels are not susceptible to degradation by proteases(*33*) and are nanoporous, it is expected that the expanding protrusion must physically open a channel in the hydrogels. To confirm this expectation and visualize the associated matrix deformation, matrix displacements were assessed using fluorescent microbeads embedding in the hydrogels. During protrusion expansion, microbeads adjacent to the protrusion moved away from the protrusion, indicating outward force generation by the protrusion (Fig. 2E, F, Movie S3). Further, when MSCs were cultured in fluorescently labelled alginate hydrogels, alginate accumulated around the length of the protrusion, confirming that protrusion expansion opened a hole in hydrogels (Fig. 2G, H). These observations indicate that MSCs expand protrusions mechanically in viscoelastic matrices in order to create channels to subsequently migrate through.

A nuclear piston drives protrusion expansion

After finding that expansion of the protrusion generates force to open a migration path in the viscoelastic and plastic hydrogels, we sought to identify the mechanisms driving protrusion volume expansion. Interestingly, prior to the expansion of the protrusion, it was consistently observed that the nucleus moves

towards and into the narrow entrance of the thin protrusions (Fig. 3A, Movie S4). A previous study found that during lobopodial-based migration, the nucleus physically compartmentalizes the cytoplasm and can be pulled towards the front compartment of the cell, functioning as a piston to cause an increase the hydrostatic pressure in that compartment(*14*, *15*). These observations implicate a potential mechanism driving protrusion expansion: entry of the nucleus into the narrow protrusion increases hydrostatic pressure in the protrusion and causes expansion of the protrusion. This potential mechanism was investigated. Blebs, which occur when increased intracellular pressure drives delamination of the membrane from the actin cytoskeleton(*34*), were often observed at the cell membrane in protrusions following entry of the nucleus into the protrusion indicating enhanced pressure in the protrusion (Fig. 3A, Movie S5). Actomyosin contractility along with the intermediate filament protein vimentin and the nucleoskeleton-intermediate filament linker protein nesprin-3 were previously found to be involved in pulling the nucleus forward and pressurizing the front of the cell(*15*). Thus, the roles of vimentin and nesprin3 in protrusion expansion and migration were first tested using small interfering RNA (siRNA) to reduce expression (fig. S3A). Nuclear location in the cell body was polarized toward the entrance of the protrusion in control cells and cells with reduced expression of nesprin-3, but not in cells with reduced expression of vimentin (Fig. 3B, C, fig. S3B, C). In addition, the loss of nuclear movements toward the protrusion with reduction of vimentin was accompanied by diminished protrusion expansion and consequently inhibited the migration of the cells, establishing the role of vimentin in the nuclear piston (Fig. 3D, E, H-J, fig. S3D, E). Vimentin is connected to lamin A/C of the nucleus(*35*) and lamin A/C is also a key element regulating nuclear shape and rigidity during 3D migration(*13*, *36*). The role of lamin A/C in protrusion expansion and migration via the nuclear piston was examined using siRNA. Decreased lamin A/C expression in cells diminished protrusion expansion and migratory behaviors of cells (Fig. 3F-J, fig.S3A). Since nuclear movements are facilitated by both actomyosin contractility(14) and microtubules(15, 34), we also examined whether these actively participate in the nuclear piston behavior observed here. Inhibition of microtubule polymerization, with nocodazole, and actomyosin contractility, with myosin inhibitor ML-7, induced the loss of nuclear polarization (Fig. 4A-C). Further, each inhibition significantly reduced the migration of cells in 3D microenvironments (Fig. 4E-F). Real-time inhibition of microtubule formation or actomyosin contractility in protruding cells resulted in an immediate relaxation of nucleus position from the entrance of the protrusion

towards the center of the cell and simultaneously decreased the width of protrusion (Fig. 4G-J). Together, these results establish that a nuclear piston, mediated by actomyosin contractility, microtubules, vimentin and lamin A/C, drives increased pressure in protrusions and subsequent protrusion expansion for migration in confining and plastic microenvironments.

Nuclear piston activates ion channels to induce ion influx into protrusions

We next sought to elucidate the molecular mechanisms connecting the nuclear piston to volume expansion of the protrusion. A simple nuclear piston mechanism could be expected to lead to water efflux from the protrusion due to the increased hydrostatic pressure. This is the opposite of what is observed, suggesting a more complex picture. It is known that cell volume can be altered by osmotic pressure, which is driven by the difference of ions concentrations between the inside and outside of the cell membrane(*37*). Therefore, ion concentrations were analyzed in expanding protrusions. Sodium and calcium imaging revealed that both sodium and calcium ion concentrations increased along the length of the protrusion, with the highest concentrations found at the tip of protrusion (Fig. 5A-D). Live-cell calcium imaging revealed that intracellular calcium ion concentration at the tip of the protrusion increased over time (Fig. 5E, F). These implicate that influx of calcium and sodium ions at the protrusion tip increases the concentration of ions within the protrusion over time. To determine the underlying mediators of differences in ions along the protrusion, we looked at the distribution of sodium and calcium channels. Since previous studies have shown that the polarized distribution of intracellular sodium ions can be driven by polarized distribution of the sodium hydrogen exchanger-1(NHE)(*18*), the distribution of NHE-1 ion channels along a protrusion was examined. The NHE-1 ion channels are more densely distributed at the tip of protrusion, similar to the distribution of intracellular sodium ion along the protrusion (fig. S4A, B). Next, the distribution of transient receptor potential vanilloid-4 (TRPV4) calcium ion channels was investigated, since we previously found that mechanosensitive TRPV4 ion channels regulate MSCs volume and work as a molecular sensor of matrix viscoelasticity in MSCs(*10*). TRPV4 calcium ion channels were evenly distributed along the protrusions, even though intracellular calcium ions showed a concentration gradient (fig. 4C, D). However, ß1 integrin membrane receptors, which can interact with and activate TRPV4 ion channels(*38*), exhibited a polarized distribution along the protrusion similarly to that of intracellular calcium ions (fig. S4C, D). To directly

assess the role of NHE-1 and TRPV4 ion channels in mediating an ion concentration gradient along the protrusion, small molecule inhibitors EIPA and GSK205 were applied to inhibit the function of NHE-1 and TRPV4, respectively. When the function of NHE-1 ion channels was inhibited, the polarized distribution of NHE-1 ion channels along the protrusion disappeared and the distribution profile of sodium ions was reversed (Fig. 5G, H, fig. S5A-C). Sodium ions were relatively high at the beginning and low at the end of the protrusion. Similarly, TRPV4 inhibitors also inverted the concentration profile of calcium ions, decreasing the calcium ion concentration at the leading edge of protrusion (Fig. 5I, J). These reversed concentration profiles of calcium ions and sodium ions by each inhibition might be due to the diffusion of ions from the cell body, which have relatively higher concentrations of ions adjacent to the nucleus. Further, the impact of the function of NHE-1 and TRPV4 ion channels on migration in 3D microenvironments was analyzed with siRNA knockdowns. Cell tracking analysis indicates that both cells in fast relaxing and plastic hydrogels migrate with slower speed and less persistence when NHE-1 or TRPV4 are knocked down, relative to control cells (Fig. 5K-N). Together, these results indicate that calcium and sodium ions flow in through NHE-1 and TRPV4 ion channels to drive protrusion expansion for migration in 3D confining environments.

We next hypothesized that the nuclear piston, or movement of the nucleus into the protrusion, serves as the key driver of ion flow into the protrusion. It is known that TRPV4 ion channels are mechanosensitive and the movement of the nucleus into the protrusion is expected to push cytoplasmic fluid into the protrusion, which pressurizes the protrusion, as indicated by the blebs, and potentially stretches the membrane. Further, it was consistently observed that movement of the nucleus into the protrusion was highly correlated with both protrusion expansion and calcium ion accumulation at the tip of the protrusion (Fig. 6A, fig. S6A, B, C). To assess our hypothesis, the distribution of intracellular calcium ion along the protrusion was analyzed in the vimentin and nesprin-3 knockdown cells. In vimentin knockdown cells, which exhibited loss of nuclear piston and diminished protrusion expansion, the distribution profile of calcium ions was reversed compared to control cells, with the calcium ion concentration at the leading edge of protrusion in cells decreasing (Fig. 6B, C). No change in calcium ion concentration in nesprin-3 knockdown cells, which exhibited normal nuclear piston and protrusion expansion, relative to control cells was observed (fig. S7A, B). Taken together, these results suggest that the nuclear piston movement increases intracellular pressure

in the protrusion, which activates mechanosensitive ion channels to flow ions in the end of protrusion, driving the protrusion expansion.

Theoretical modeling and experiments show that increased osmotic pressure outcompetes hydrostatic pressure to drive protrusion expansion

To better understand the underlying physics of the nucleus-driven expansion of protrusion, and the competition between increased hydrostatic pressure in the protrusion, which would promote water efflux, and increased osmotic pressure in the protrusion, which would promote water influx, we developed a theoretical model (Fig. 6D). With the nuclear movement, the fluid in front of the nucleus is pushed into the protrusion in a piston-like manner. Subsequently, the hydrostatic pressure in the protrusion, P_{in}, increases and the protrusion membrane is stretched which in turn activates stretch-mediated ion channels on the protrusion membrane (Fig. 6D, E). With the opening of the mechanosensitive channels, ions can flow in and out of the protrusion in the direction of the ion concentration gradient across the membrane (Fig. 6D, E). The ion flux rate (dn/dt) is determined by the difference between the osmotic pressures outside (Π_{out}) and inside (Π_{in}) of the protrusion (Fig. 6D, E). On the other hand, the protrusion expansion rate ($dr/dt = J_1 + J_2 + J_3$) is determined by the influx and efflux of fluid where J_1, J_2, and J_3 are respectively governed by (i) the rate of fluid transport to the protrusion by the nuclear movement, (ii) the hydrostatic pressure difference across the membrane, and (iii) the osmotic pressure difference across the membrane (Fig. 6D, E). Note that the ion flux rate and the protrusion expansion rate are mutually dependent (see Methods).

With this model of the nuclear piston that incorporates fluid transport due to the piston, hydrostatic pressure, and osmotic pressure, we ran the model and validated the model with experiments (Fig. 7A). The model predicts that the activation of mechanosensitive ion channels, upon pressurizing the protrusion by the nuclear piston, allows an influx of ions into the protrusion which in turn increases osmotic pressure in the protrusion to oppose the efflux of fluid (fig. S8B-F, H-L). This leads to a positive net amount of fluid flow into the protrusion (fig. S8G, M) and subsequently an expansion of the protrusion which is in excellent agreement with our experimental observation (Fig. 7B, C). Further, the model predicted that in the absence of protrusion ion channels, cell protrusions cannot expand as the fluid influx J_1 is almost equal to the fluid efflux $J_2 + J_3$

|. This prediction is consistent with experimental observations where inhibition of the ion channels or chelating of intracellular calcium ions prevents the expansion of protrusion (Fig. 7B-D, fig. S8B-F, H-L). It should be noted that while protrusion expansion, as well as cell migration speed and track length, were decreased by inhibiting ion channels or chelating intracellular ions (Fig. 7E, fig. S9), protrusion lengthening was not impeded, indicating that other mechanisms regulate the initial extension of the thin protrusion (Fig. 7F).

Next, the model predicted the anticipated results of real-time inhibitions of mechanosensitive ion channels and actomyosin contractility (Fig. 7G, fig. S10A-G). After the initial expansion of the protrusion due to the forward movement of the nucleus, the model predicts that the inhibition of mechanosensitive ion channels reduces the osmotic pressure in the protrusion (fig. S10F), so that the radius of the protrusion mildly decreases (Fig. 7H). Also, the model predicts that the nucleus continues its forward movement (Fig. 7I) as the posterior hydrostatic pressure remains higher than the hydrostatic pressure in the protrusion (fig. S10E). Likewise, the experimental observations exhibited that TRPV4 inhibition in real-time did not impact nuclear movements but did prevent the influx of ions. As a result, the radius of the protrusion decreased over time, indicating the nuclear piston to be upstream of ion channel activation (Fig. 7H-J). On the other hand, the model predicted that real-time inhibition of the contractility led to a significant drop in the posterior hydrostatic pressure (fig. S10E), thus the nucleus moved backward (Fig. 7I) and the protrusion width decreased (Fig. 7K). These predictions were both in agreement with the experimental observations (Fig. 7H, I, K). Thus, the model and the experimental results elucidate how the nuclear movement, the influx/efflux of ions, and intracellular fluid work in concert to control the protrusion volume through balancing the hydrostatic and osmotic differences across the membrane.

Discussion

Together, our data from experiments and simulations reveal the physical mechanisms of how stem cells generate paths to migrate in confining viscoelastic and plastic matrices, which have no pre-existing migration path (Fig. 8). MSCs initially generate shallow protrusions into the matrices. Then, the nucleus is pushed into the protrusion like a piston, increasing intracellular pressure in the protrusion. Actomyosin contractility,

vimentin, and microtubules are involved in the nuclear piston, which activates mechanosensitive ion channels to flow ions in the end of protrusion, balancing the osmotic pressure between inside and outside of protrusion. Finally, the increased osmotic pressure in the protrusion reduces water efflux, promoting the expansion of the protrusion, which physically opens up a migration path in the confining viscoelastic and plastic microenvironments.

Here we found that cells migrate in viscoelastic and plastic matrices that are nanoporous, but not in matrices that were more elastic. Most natural ECMs are viscoelastic, exhibiting some degree of fluid-like behaviors and stress relaxation in response to a deformation, and viscoplastic, exhibiting irreversible deformations in response to mechanical stress or strain (*5*, *39*, *40*). In the type-1 rich collagen networks that provide mechanical support to many soft tissues, unbinding of weak bonds between fibers or between fibrils within a fiber, followed by matrix flow or sliding of fibrils and then rebinding of weak bonds, represent two sources of viscoelasticity and viscoplasticity, though many other mechanisms likely contribute (*41–43*). Covalent crosslinks act to diminish viscoelasticity and plasticity. We have previously shown that matrix viscoelasticity and plasticity in 3D regulates processes that involve shape or volume change such as mediate cell volume expansion, matrix deposition, cell-cycle progression and mitosis, matrix remodeling, and migration of cancer cells(*5*, *10*, *28*, *30*, *40*, *44*, *45*). Particularly relevant to this study, we previously showed that matrix mechanical plasticity regulated the probability of protrusion formation and extension, and cell migration, with a sufficient level of matrix mechanical plasticity enabling protrusion formation, protrusion extension, and migration (*28*). Consistent with this idea, here we show that matrix viscoelasticity and viscoplasticity regulate the migration of stem cells.

Our finding that MSCs use the nuclear piston to generate a migration path in confining matrices adds a fresh new insight into our current understanding of migration path generation. For rigid pore sizes with a diameter below ~ 3 μm, it is known that cancer cells and fibroblasts are unable to squeeze their stiff nucleus through the pore (*12*, *13*). For immune cells, the minimum pore size for migration is lower, but the same principle applies. Thus, extracellular matrices with smaller pore sizes are considered to be confining with cells having to generate a micron-size path in order to migrate. Smaller pore sizes are likely to be relevant to many, if not most, extracellular matrices. However, the topic of migration path generation has been largely avoided in previous studies of confined cell migration, which often utilize microfabricated

channels where migration paths are pre-defined (*16–18*, *21–25*, *46–48*). In matrices that are degradable, cells can secrete MMPs or other proteases to biochemically degrade the matrix and help form migration paths, and much is known about these mechanisms (*12*, *19*, *20*, *26*, *27*). We previously found that cancer cells can migrate through nanoporous matrices that exhibit sufficient mechanical plasticity (*28*). Here we show that the nuclear piston is used to expand protrusions and generate migration paths in viscoelastic and viscoplastic matrices, independent of protease activity. From the mechanism of nuclear translocation, we found that nuclear piston movements generate a migration path by increasing pressure in the shallow protrusion. Membrane blebs, and an increase in calcium concentration in the protrusion through mechanically activated ion channels, are associated with the forward movement of the nucleus and indirectly indicate the increase of pressure in the protrusion due to the nuclear piston. Further, the alginate accumulation and the dislocations of embedded microbeads around the expanding protrusion directly show that protrusion expansion generates a migration path. As biological matrices are both susceptible to degradation and are viscoelastic/viscoplastic, it is possible that the nuclear piston mechanism acts synergistically with known protease-dependent modes of migration path generation.

Mechanistically, we find some distinctions between the nuclear piston used by MSCs in confining hydrogels, and the nuclear piston mechanism described previously. Previous studies demonstrated that vimentin and nesprin-3, one of LINC proteins, are important components that mediate nuclear piston movement during lobopodial-based migration by cancer cells and fibroblasts in microporous collagen gels (*14*, *15*). Surprisingly, we found that nesprin-3 is not directly involved in the nuclear piston movements for MSCs in nanoporous alginate hydrogels. The nesprin family is composed of four nesprins, so it is possible that another nesprin might be involved in the nuclear piston in MSCs. We do find that lamin A/C proteins are necessary for protrusion expansion and the nuclear piston mechanism. Since the lamin A/C proteins serve as a key link between the LINC complex and the nucleus, these findings are suggestive of force transmission through the nucleus during this process. In addition, while previous studies implicated actomyosin contraction at the anterior part of the cell (i.e. protrusion) as the main mechanism pulling the nucleus into the protrusion (*14*, *15*), our results indicate that actomyosin in the posterior part of the cell may be more activated than actomyosin in the anterior part. Similar to our observation, a recent study showed that elevated contractility at the cell posterior for cancer cells in confining channels locally increases

cytoplasmic pressure and promotes nuclear translocation and bleb formation(*49*). Collectively, these results indicate that the nuclear piston mechanism for generating the migration paths may have various different flavors, which might be dependent on cell type and whether the microenvironment is fully confining, microporous, or channel-like.

In addition, the identification of mechanosensitive ion channels in cell migration adds the known list of key molecular players driving the nuclear piston and involved in cell migration generally. It was known that the nuclear piston mechanism involved actomyosin contractility, vimentin, and nesprin-3 to pull the nucleus forward and pressurize the front of the cell (*14*, *15*). We show that mechanosensitive ions subsequently play a critical role in driving the osmotic pressure changes that overcome the increase in hydrostatic pressure in the protrusion to drive protrusion expansion. While we focused on TRPV4 and NHE-1, a recent study found that the mechanosensitive ion channel TRPM7 plays a central role in how cancer cells sense hydraulic pressure and cross sectional area in microfabricated microchannels (*24*). This suggests that other mechanosensitive ion channels could also be involved in regulating the nuclear piston. Together, these findings highlight the important, and previously underappreciated, role of mechanosensitive ion channels in cell migration.

Finally, our finding that matrix viscoelasticity and plasticity facilitate the migration of stem cells has broad implications for the design of biomaterials in clinical applications. Various applications in regenerative medicine involve the delivery of stem cells, or recruitment of local host cells (*50*). Further, the emerging field of biomaterials-based immunoengineering often involves the use of biomaterials to recruit, infiltrate, and program immune cells (*51*). Thus, our findings point towards hydrogel viscoelasticity and viscoplasticity as a critical design parameter that can be modulated to optimize performance in such applications.

Materials and Methods

Alginate preparation

Sodium alginate (average molecular weight; 280 kDa, high-MW, Protanal LF 20/40, FMC Biopolymer) was used directly for the high-MW alginate gels. This alginate was also modified by irradiation with a 8 Mrad cobalt source to produce low molecular weight (low-MW) alginates (average molecular weight; 35 kDa)(*52*). RGD oligopeptides coupled to the alginates using standard carbodiimide chemistry(*52*). The alginates were reconstituted at 1% wt/vol in 0.1M MES buffer. Sulfo-NHS (ThermoFisher Scientific), N-(3 dimethylaminopropyl)-N′-ethylcarbodiimide (EDC, Sigma-Aldrich) and RGD oligopeptide (GGGGRGDSP, peptide 2.0) were sequentially added in the alginate solution, and then the reaction continued for 20 hours until adding hydroxylamine hydrochloride (Sigma) to quench. The alginate was dialyzed in deionized water for 2~3 days, purified with activated charcoal, sterile-filtered, lyophilized, and stored in a -20C freezer until it was used. For cell encapsulation, alginate was reconstituted at 3% wt/vol in serum-free Dulbecco's modified Eagle's medium (DMEM, Life Technologies). The final concentration of RGD peptide in the 2% w/v alginate hydrogels was 1500 μM. For preparation of fluorescent alginates, fluorescein amine isomer (Acros Organics) was coupled to RGD coupled alginate using carbodiimide chemistry at a concentration of 37.74 μM as described above.

Mechanical characterization

Unconfined compression tests were made with an Instron 5848 mechanical tester (Instron)(*30*). Alginate hydrogels and PEG hydrogels for compression characterization were prepared with disk shaped hydrogels (6-mm in diameter and 2-mm thick). The disks of hydrogels were incubated overnight in Dulbecco's Modified Eagles Medium (DMEM, Invitrogen). The samples were compressed with a rate of 1 mm/min until 15% strain and held constant. Stress and strain of the hydrogels was recorded over time. The initial modulus of the hydrogel was calculated with the slope of stress–strain curve between 5 and 10% strain. The time of stress relaxation of each alginate ($\tau_{1/2}$) was measured as the time for which the initial stress at 15% strain decreased to half of its original value. The stress relaxation profile of a human fracture hematoma in Fig. 1C was obtained from previously published work(*5*). Since volume of the gels or fluid flow out of the gel does not occur in shear, shear relaxation tests were conducted with an AR-G2 rheometer to show

differences in stress relaxation only due to ionic crosslinker unbinding and polymer flow, and not the fluid flow out of the samples(*30*). For sample preparation, the mixtures of alginate hydrogels were directly deposited between two plates of the rheometer as soon as mixing. After fully gelling the alginate mixtures indicated by reaching an equilibrium of both loss and storage modulus, a constant shear strain of 15% strain were then applied for 10,000s and measure stress relaxation property of hydrogels.

Mechanical plasticity of the hydrogels was characterized using creep-recovery tests in a rheometer(*40*). Hydrogel samples for plasticity tests were prepared by directly depositing alginate solutions between two plate of the rheometer immediately after mixing, prior to gelation. To prevent the dehydration of hydrogel, mineral oil (Sigma) was applied to the surface of the gel disk at the edge of plates. Gelation was tracked by periodically recording the storage and loss modulus. After the storage modulus reached an equilibrium value, this time sweep was followed by a creep-recovery test. First, a constant shear stress (150 Pa) was applied for 3600s and then unloaded (0 Pa) for 6400 s (1.7 h) to recover the samples from the absence of stress. The strain derived from loading and unloading stress was recorded as a function of time. The plasticity of each hydrogel was measured with the ratio of strain after recovery test to the maximum strain at the end of loading.

Encapsulation cells in hydrogels

D1 MSCs (CRL-12424, ATCC) were cultured to 70% confluency and encapsulated in alginate hydrogels. Cells were trypsinized with 0.05% trypsin/EDTA, washed with DPBS, centrifuged, and resuspended in growth medium containing 10% fetal bovine serum (FBS, GE Healthcare). The number of cells was counted using a Vi-Cell Coulter counter (Beckman Coulter). Cells were homogeneously mixed with the alginate solution prior to adding calcium crosslinkers (CaSO4). The final cell concentration was 10 million cells/mL in the cell-laden mixture. The mixture was then deposited between two glass plates spaced a 1mm apart. The hydrogels were allowed to gel for 45mins, and then disks of hydrogel were punched our using a biopsy punch. The hydrogel disks containing cells were then cultured in gels for 1 to 2 days in induction medium containing 50 μg/ml L-ascorbic acid (MilliporeSigma), 10 mM β-glycerophosphate (MilliporeSigma), and 0.1 μM dexamethasone (MilliporeSigma). After one day, bright field microscopy was used to capture cell morphologies. For visualizing displacement of hydrogels, fluorescent alginates were used, instead of normal alginate or fluorescent microbeads (Thermofisher, Cat# F8811) were added into the cell-alginate mixture.

Live cell imaging

For live-cell studies using D1 MSCs in alginate, samples were prepared with a procedure similar to above. For migration studies, the membranes of MSCs were labelled with octadecyl rhodamine B chloride (1:1000 dilution, R18, ThermoFisher Scientific) prior to encapsulating cells in alginate. The stained cell-laden alginate hydrogels were punched out, transferred into the wells of a chambered coverglass (LabTek), and covered with low-melting-temperature agarose (Cat# 50302, Lonza, Swiss) to prevent the hydrogel from floating. Induction medium was added in wells with vehicle alone or inhibitor. After hydrogels were fully swelled for 6 hours in an incubator, MSCs were imaged in an incubated chamber (37 °C and 5% CO2) at 15 min or 30 min intervals with a confocal microscope (Leica CM1950 20/0.40 NA objective) overnight. For imaging nucleus, a similar procedure was followed and cells in hydrogels were incubated for 1 hour with nucleus dye (Hoechst 33342, Invitrogen), washed three times with DMEM, and the hydrogels were covered with agarose for live cell imaging.

For live inhibition studies, the chambers were covered with plastic wrap to prevent dehydration of medium. Individual cells with nuclei positioned at the entrance of protrusion were marked using the mark-and-find feature of the Leica software. Small molecule inhibitors were then delivered to each wells and image multiple cells at every time point. Specific drug concentrations were described at the section of inhibition tests.

Intracellular ions imaging

For imaging intracellular ions in MSCs, both Fura-red AM (33 μM, ThermoFisher Scientific) and Fluo-3 AM (20 μM, ThermoFisher Scientific) were applied for imaging intracellular calcium(*53*, *54*) and cytosolic Na+ indicator (25 μM, ION NaTRIUM Green™-2 AM, ab142802, Abcam) were used for imaging intracellular sodium ions(*55*). Cells encapsulated in alginates hydrogels were incubated with each indicator for 1 h and washed three times with DPBS and incubated in the induction medium before live cell imaging. Intracellular ions were live imaged at 15 min or 30 min intervals with a confocal microscope (Leica CM1950 20/0.8 NA objective) overnight. Sodium ion concentration in cells were measured with the intensity of sodium indicator and calcium ion concentration was measured using the ratio of the Fluo-3 intensity to the Fura-red intensity(*53–55*).

Immunohistochemistry

For immunohistochemical staining, the cell-laden hydrogel samples were taken out of media, washed in PBS containing calcium (cPBS, GE), and fixed with 4% paraformaldehyde (Alfa Aesar) in DMEM at room temperature for 45-60 min. Then, the samples were washed three times in PBS containing calcium, incubated in 30% sucrose (Fisher Scientific) in cPBS overnight, and then placed in OCT-sucrose mixture, containing 50% OCT (Tissue-Tek, Sakura) and the other 50% of a 30% sucrose solution, for 4 h. The samples were then embedded in OCT and frozen. The gels were then sectioned with a thickness of 30-60 μm using a cryostat (Leica CM1950), and the staining processed using standard immunohistochemistry protocols.

The following antibodies and reagents were applied for immunohistochemistry: anti-NHE-1 (1:200; ab67314, Abcam), anti-TRPV4 (1:200; ab39260, Abcam), anti-β1 integrin (1:300; ab24693, Abcam), anti-Vimentin (1:200; ab92547, Abcam), anti-Nesprin3 (1:200; ab74261, Abcam), anti-Alpha tubulin (1:200; DM1A, Cell signaling), and Phospho Myosin Light Chain (1:200; ab3381, Millipore Sigma). DAPI(1:1000, Invitrogen) and AF-488 Phalloidin (1:80, Invitrogen) were used to stain the nucleus and the actin cytoskeleton, respectively. The following secondary antibodies were used: Goat anti-Rabbit IgG AF 647 (Invitrogen), Goat anti-Mouse IgG AF 647 (Invitrogen), Goat anti-Rabbit IgG AF 555(Invitrogen) and Goat anti-Mouse IgG AF 555(Invitrogen). Prolong Gold antifade reagent (Life Technologies) was applied to prevent photobleaching.

Inhibition/siRNA knockdown tests

For inhibition the function of TRPV4 and NHE ion-channels, GSK205 (10 μM(*10*, *56*), Calbiochem) and EIPA (20 μM(*18*), R&D system) were applied, respectively. Bapta-AM (10 μM(*24*, *57*), ThermoFisher) was used to chelate intracellular calcium ions in MSCs. For inhibition microtubule polymerization and myosin activity, Nocodazole (10 μM(*15*, *16*), Tocris Bioscience) and ML-7 (25 μM(*5*, *10*), Tocris Bioscience) were applied to the induction media, respectively. Inhibitor concentrations were based on those used in previous studies.

For knocking down the expression of vimentin and nesprin3, MSCs were transfected with 50 nM vimentin siRNA SMARTpool (L-061596-01-0010, Dharmacon), 50 nM Syne3 siRNA SMARTpool (L-052180-01-

0010, Dharmacon), 50nM NHE-1 siRNA SMARTpool (L-048336-01-0020, Dharmacon), 50nM TRPV4 siRNA SMARTpool (L-040742-00-0020, Dharmacon), and 50nM Lamin A/C siRNA SMARTpool (L-040758-00-0020, Dharmacon), respectively. Control cells was transfected with ON-TARGETplus Non-Targeting Control Pool (D-001810-10-20, Dharmacon). All cells were transfected for 3 days using DharmaFECT Transfection Reagent (T-2001-01, Dharmacon) and knockdown efficiency was analyzed by Western blotting.

Western blot

siRNA transfected cells were extracted and centrifuged. Cell pellets were lysed in Pierce RIPA buffer (89900, ThermoFisher) with Protease Inhibitor Cocktail Tablets (11836170001, Roche) and PhosSTOP Phosphatase Inhibitor Cocktail Tablets (04906845001, Roche). The protein concentration in each sample was measured using the Pierce BCA Protein Assay Kit (23227, Thermo Fisher). Laemmli Sample Buffer (1610747, Bio-Rad) was used to dilute samples to 3.5 µg/µl. 35 µg of total protein was added in each lane of a 4-15%, 15-well gradient gels (4561086, Bio-Rad). The gels were run for 35 min and the proteins were transferred to nitrocellulose (Bio- Rad) at 100V for 45 mins. The membrane was blocked in 5% milk for 1 h, incubated overnight in primary antibodies against Vimentin (ab92547, Abcam, 1:1000), Nesprin3 (ab74261, Abcam, 1:500), Lamin A/C (2032S, Cell Signaling, 1:1000), NHE-1 (SC-136239, Santa Cruz Biotechnology, 1:1000), TRPV4(ab39260, Abcam, 1:1000), P38 (SC-535, Santa Cruz Biotechnology, 1:1000) and GAPDH (ab181602, Abcam, 1:1000). Blots were incubated with secondary antibodies against the primary for 1hour and imaged using a Licor Odyssey imaging system (LI-COR Biotechnology).

3D image analysis

To measure cell volume and sphericity, cells in hydrogels were fixed with 4% paraformaldehyde and stained with R18 and DAPI. 3D image stacks were taken using a confocal microscope (Leica SP8, PL APO 63X/1.4 NA oil immersion objective) with a 0.5µm z-axis interval(*10*). The image stacks were visualized using a constant threshold for each experiment. Cell volumes and sphericity were automatically calculated using Imaris software(*10*).

Cell body and protrusion were distinguished by following procedure: first, we found the maximum width of the entire cell and drew the largest ellipsoid which is located inside the cell and has the center at the middle of the maximum width. The ellipsoid was regarded as cell body and the rest of the cells was considered to be a protrusion.

Body volume was calculated with 3D image stack at which the body area was marked by hand-tracing in each slice. Protrusion volume was measured by subtracting the body volume from entire volume.

To compare protrusion volume to width, the identical image stacks were used to measure the protrusion volume and width. The 3D image stacks were converted into a 2D image by accumulating all images. The protrusion width was then measured at the middle of the protrusion with the accumulated 2D images and the protrusion length was measured with a line following the protrusion from leading edge of protrusion to the edge of body part.

For live cell images to take 3D stacks, labeled cells in hydrogels were imaged using confocal microscope (Leica SP8, A 20X/0.8 NA dry objective). The 3D stacks for live cell imaging were taken with 1μm z-axis interval by considering pixel distance of x–y plane.

To measure track length and speed of migration in 3D hydrogels, 3D stack images were recorded with 5-10μm z-axis interval for 20 hours and the cell centroids in the 3D stack images were tracked using Imaris software. Track length and speed of migration were automatically calculated by Imaris software. Migration trajectories were reconstructed with a custom MATLAB code.

2D image analysis

For measuring the distribution of intracellular ion and proteins, ImageJ was used with the 2D image accumulating all slices of 3D stack images. The distribution profiles were obtained by measuring signal intensity profile of each targets. Along the protrusion, the intensity profiles were measured 3 times with a line following the protrusion from leading edge of protrusion to the edge of body part.

Nuclear location in the cell body was measured using ImageJ with DAPI and phalloidin signals. As described above, body area in entire single cell was found with the ellipsoid and the center of the ellipsoid was regarded as the center of the body. The centroid of nucleus was found with DAPI signal. A vector was then obtained from the center of cell body to the center of nucleus. Another vector was obtained from the center of cell

body to the middle of protrusion entrance. Polarization of nuclear location in cell body was calculated as the angle between these two vectors.

For mapping the displacement of matrix, drift of fluorescent microbeads image was corrected using ImageJ and microbeads embedded in hydrogels in images were tracked with a particle image velocimetry (PIV) plugin in ImageJ (PIVlab; MATLAB) using three cross-correlation windows (128 × 128, 64 × 64 and 32 × 32 pixel-size interrogation window). The mesh sizes of the windows were manually chosen accordingly for the local bead concentration. The results from this PIV analysis provided a vector field of matrix displacements and a heat map. The control was quantified by measuring the dislocation of beads located at the 30 μm away from each cell.

The accumulation of matrix was measured as the ratio intensity of fluorescent alginate within 2 μm of the border of protrusion to the intensity of the background hydrogel at 30 μm away from each cell. The control was quantified as the ratio intensity of fluorescent alginate within 10 μm of the cell border to the background intensity of the hydrogel.

Statistical analysis

GraphPad prism was used for all statistical analyses. Specific method of statistics, P values, and sample numbers of each comparisons are reported in figure legends. All quantifications for statistical analysis were from at least three independent experiments with two biological replicates per experiment.

References and Notes

1. W. Lin, L. Xu, S. Zwingenberger, E. Gibon, S. B. Goodman, G. Li, Mesenchymal stem cells homing to improve bone healing. *J. Orthop. Transl.* **9**, 19–27 (2017).
2. N. Huebsch, E. Lippens, K. Lee, M. Mehta, S. T. Koshy, M. C. Darnell, R. M. Desai, C. M. Madl, M. Xu, X. Zhao, O. Chaudhuri, C. Verbeke, W. S. Kim, K. Alim, A. Mammoto, D. E. Ingber, G. N. Duda, D. J. Mooney, Matrix elasticity of void-forming hydrogels controls transplanted-stem-cell-mediated bone formation. *Nat. Mater.* **14**, 1269–1277 (2015).
3. P. Su, Y. Tian, C. Yang, X. Ma, X. Wang, J. Pei, A. Qian, Mesenchymal stem cell migration during bone formation and bone diseases therapy. *Int. J. Mol. Sci.* **19** (2018), doi:10.3390/ijms19082343.
4. C. Loebel, J. A. Burdick, Engineering Stem and Stromal Cell Therapies for Musculoskeletal Tissue Repair. *Cell Stem Cell*. **22**, 325–339 (2018).
5. O. Chaudhuri, L. Gu, D. Klumpers, M. Darnell, S. A. Bencherif, J. C. Weaver, N. Huebsch, H. P. Lee, E. Lippens, G. N. Duda, D. J. Mooney, Hydrogels with tunable stress relaxation regulate stem cell fate and activity. *Nat. Mater.* **15**, 326–334 (2016).
6. O. Chaudhuri, J. Cooper-White, P. A. Janmey, D. J. Mooney, V. B. Shenoy, Effects of extracellular matrix viscoelasticity on cellular behaviour. *Nature*. **584**, 535–546 (2020).
7. Z. Gong, S. E. Szczesny, S. R. Caliari, E. E. Charrier, O. Chaudhuri, X. Cao, Y. Lin, R. L. Mauck, P. A. Janmey, J. A. Burdick, V. B. Shenoy, Matching material and cellular timescales maximizes cell spreading on viscoelastic substrates. *Proc. Natl. Acad. Sci. U. S. A.* **115**, E2686–E2695 (2018).
8. J. Lou, R. Stowers, S. Nam, Y. Xia, O. Chaudhuri, Stress relaxing hyaluronic acid-collagen hydrogels promote cell spreading, fiber remodeling, and focal adhesion formation in 3D cell culture. *Biomaterials*. **154**, 213–222 (2018).
9. A. R. Cameron, J. E. Frith, G. A. Gomez, A. S. Yap, J. J. Cooper-White, The effect of time-dependent deformation of viscoelastic hydrogels on myogenic induction and Rac1 activity in mesenchymal stem cells. *Biomaterials*. **35**, 1857–1868 (2014).
10. H. pyo Lee, R. Stowers, O. Chaudhuri, Volume expansion and TRPV4 activation regulate stem cell fate in three-dimensional microenvironments. *Nat. Commun.* **10** (2019), doi:10.1038/s41467-019-08465-x.
11. C. Loebel, R. L. Mauck, J. A. Burdick, Local nascent protein deposition and remodelling guide mesenchymal stromal cell mechanosensing and fate in three-dimensional hydrogels. *Nat. Mater.* **18**, 883–891 (2019).
12. K. Wolf, M. te Lindert, M. Krause, S. Alexander, J. te Riet, A. L. Willis, R. M. Hoffman, C. G. Figdor, S. J. Weiss, P. Friedl, Physical limits of cell migration: Control by ECM space and nuclear deformation and tuning by proteolysis and traction force. *J. Cell Biol.* **201**, 1069–1084 (2013).
13. T. Harada, J. Swift, J. Irianto, J. W. Shin, K. R. Spinler, A. Athirasala, R. Diegmiller, P. C. D. P. Dingal, I. L. Ivanovska, D. E. Discher, Nuclear lamin stiffness is a barrier to 3D migration, but softness can limit survival. *J. Cell Biol.* **204**, 669–682 (2014).
14. R. J. Petrie, H. M. Harlin, L. I. T. Korsak, K. M. Yamada, Activating the nuclear piston mechanism of 3D migration in tumor cells. *J. Cell Biol.* **216**, 93–100 (2017).
15. R. J. Petrie, H. Koo, K. M. Yamada, Generation of compartmentalized pressure by a nuclear piston governs cell motility in a 3D matrix. *Science (80-.).* **345**, 1062–1065 (2014).
16. J. Renkawitz, A. Kopf, J. Stopp, I. de Vries, M. K. Driscoll, J. Merrin, R. Hauschild, E. S. Welf, G. Danuser, R. Fiolka, M. Sixt, Nuclear positioning facilitates amoeboid migration along the path of least resistance. *Nature*. **568**, 546–550 (2019).
17. Y. J. Liu, M. Le Berre, F. Lautenschlaeger, P. Maiuri, A. Callan-Jones, M. Heuzé, T. Takaki, R. Voituriez, M. Piel, Confinement and low adhesion induce fast amoeboid migration of slow mesenchymal cells. *Cell*. **160**, 659–672 (2015).

18. K. M. Stroka, H. Jiang, S. H. Chen, Z. Tong, D. Wirtz, S. X. Sun, K. Konstantopoulos, Water permeation drives tumor cell migration in confined microenvironments. *Cell*. **157**, 611–623 (2014).
19. K. M. Schultz, K. A. Kyburz, K. S. Anseth, Measuring dynamic cell-material interactions and remodeling during 3D human mesenchymal stem cell migration in hydrogels. *Proc. Natl. Acad. Sci. U. S. A.* **112**, E3757–E3764 (2015).
20. E. Infante, A. Castagnino, R. Ferrari, P. Monteiro, S. Agüera-González, P. Paul-Gilloteaux, M. J. Domingues, P. Maiuri, M. Raab, C. M. Shanahan, A. Baffet, M. Piel, E. R. Gomes, P. Chavrier, LINC complex-Lis1 interplay controls MT1-MMP matrix digest-on-demand response for confined tumor cell migration. *Nat. Commun.* **9** (2018), doi:10.1038/s41467-018-04865-7.
21. A. Reversat, F. Gaertner, J. Merrin, J. Stopp, S. Tasciyan, J. Aguilera, I. De Vries, R. Hauschild, M. Hons, M. Piel, A. Callan-jones, R. Voituriez, M. Sixt, Cellular locomotion using environmental topography. *Nature* (2020), doi:10.1038/s41586-020-2283-z.
22. M. Raab, M. Gentili, H. De Belly, H. R. Thiam, P. Vargas, A. J. Jimenez, F. Lautenschlaeger, R. Voituriez, A. M. Lennon-Duménil, N. Manel, M. Piel, ESCRT III repairs nuclear envelope ruptures during cell migration to limit DNA damage and cell death. *Science (80-.).* **352**, 359–362 (2016).
23. V. Ruprecht, S. Wieser, A. Callan-Jones, M. Smutny, H. Morita, K. Sako, V. Barone, M. Ritsch-Marte, M. Sixt, R. Voituriez, C. P. Heisenberg, Cortical contractility triggers a stochastic switch to fast amoeboid cell motility. *Cell*. **160**, 673–685 (2015).
24. R. Zhao, A. Afthinos, T. Zhu, P. Mistriotis, Y. Li, S. A. Serra, Y. Zhang, C. L. Yankaskas, S. He, M. A. Valverde, S. X. Sun, K. Konstantopoulos, Cell sensing and decision-making in confinement: The role of TRPM7 in a tug of war between hydraulic pressure and cross-sectional area. *Sci. Adv.* **5**, eaaw7243 (2019).
25. C. M. Denais, R. M. Gilbert, P. Isermann, A. L. McGregor, M. Te Lindert, B. Weigelin, P. M. Davidson, P. Friedl, K. Wolf, J. Lammerding, Nuclear envelope rupture and repair during cancer cell migration. *Science (80-.).* **352**, 353–358 (2016).
26. F. Sabeh, R. Shimizu-Hirota, S. J. Weiss, Protease-dependent versus-independent cancer cell invasion programs: Three-dimensional amoeboid movement revisited. *J. Cell Biol.* **185**, 11–19 (2009).
27. P. Friedl, Prespecification and plasticity: Shifting mechanisms of cell migration. *Curr. Opin. Cell Biol.* **16**, 14–23 (2004).
28. K. M. Wisdom, K. Adebowale, J. Chang, J. Y. Lee, S. Nam, R. Desai, N. S. Rossen, M. Rafat, R. B. West, L. Hodgson, O. Chaudhuri, Matrix mechanical plasticity regulates cancer cell migration through confining microenvironments. *Nat. Commun.* **9** (2018), doi:10.1038/s41467-018-06641-z.
29. K. H. Vining, D. J. Mooney, Mechanical forces direct stem cell behaviour in development and regeneration. *Nat. Rev. Mol. Cell Biol.* **18**, 728–742 (2017).
30. H. P. Lee, L. Gu, D. J. Mooney, M. E. Levenston, O. Chaudhuri, Mechanical confinement regulates cartilage matrix formation by chondrocytes. *Nat. Mater.* **16**, 1243–1251 (2017).
31. M. Darnell, S. Young, L. Gu, N. Shah, E. Lippens, J. Weaver, G. Duda, D. Mooney, Substrate Stress-Relaxation Regulates Scaffold Remodeling and Bone Formation In Vivo. *Adv. Healthc. Mater.* **6**, 1–8 (2017).
32. N. Huebsch, P. R. Arany, A. S. Mao, D. Shvartsman, O. A. Ali, S. A. Bencherif, J. Rivera-Feliciano, D. J. Mooney, Harnessing traction-mediated manipulation of the cell/matrix interface to control stem-cell fate. *Nat. Mater.* **9**, 518–26 (2010).
33. K. Y. Lee, D. J. Mooney, Hydrogels for tissue engineering. *Chem. Rev.* **101**, 1869–1879 (2001).
34. G. T. Charras, J. C. Yarrow, M. A. Horton, L. Mahadevan, T. J. Mitchison, Non-

equilibration of hydrostatic pressure in blebbing cells. *Nature*. **435**, 365–369 (2005).
35. M. Crisp, Q. Liu, K. Roux, J. B. Rattner, C. Shanahan, B. Burke, P. D. Stahl, D. Hodzic, Coupling of the nucleus and cytoplasm: Role of the LINC complex. *J. Cell Biol.* **172**, 41–53 (2006).
36. R. de Leeuw, Y. Gruenbaum, O. Medalia, Nuclear Lamins: Thin Filaments with Major Functions. *Trends Cell Biol.* **28**, 34–45 (2018).
37. F. Lang, G. L. Busch, M. Ritter, H. Völkl, S. Waldegger, E. Gulbins, D. Häussinger, Functional significance of cell volume regulatory mechanisms. *Physiol. Rev.* **78**, 247–306 (1998).
38. B. D. Matthews, C. K. Thodeti, J. D. Tytell, A. Mammoto, D. R. Overby, D. E. Ingber, Ultra-rapid activation of TRPV4 ion channels by mechanical forces applied to cell surface β1 integrins. *Integr. Biol.* **2**, 435–442 (2010).
39. I. Levental, P. C. Georges, P. A. Janmey, Soft biological materials and their impact on cell function. *Soft Matter*. **3**, 299–306 (2007).
40. S. Nam, J. Lee, D. G. Brownfield, O. Chaudhuri, Viscoplasticity Enables Mechanical Remodeling of Matrix by Cells. *Biophys. J.* **111**, 2296–2308 (2016).
41. E. Ban, J. M. Franklin, S. Nam, L. R. Smith, H. Wang, R. G. Wells, O. Chaudhuri, J. T. Liphardt, V. B. Shenoy, Mechanisms of Plastic Deformation in Collagen Networks Induced by Cellular Forces. *Biophys. J.* **114**, 450–461 (2018).
42. S. Münster, L. M. Jawerth, B. A. Leslie, J. I. Weitz, B. Fabry, D. A. Weitz, Strain history dependence of the nonlinear stress response of fibrin and collagen networks. *Proc. Natl. Acad. Sci. U. S. A.* **110**, 12197–12202 (2013).
43. S. Nam, K. H. Hu, M. J. Butte, O. Chaudhuri, Strain-enhanced stress relaxation impacts nonlinear elasticity in collagen gels. *Proc. Natl. Acad. Sci. U. S. A.* **113**, 5492–5497 (2016).
44. S. Nam, V. K. Gupta, H. pyo Lee, J. Y. Lee, K. M. Wisdom, S. Varma, E. M. Flaum, C. Davis, R. B. West, O. Chaudhuri, Cell cycle progression in confining microenvironments is regulated by a growth-responsive TRPV4-PI3K/Akt-p27Kip1 signaling axis. *Sci. Adv.* **5** (2019), doi:10.1126/sciadv.aaw6171.
45. S. Nam, O. Chaudhuri, Mitotic cells generate protrusive extracellular forces to divide in three-dimensional microenvironments. *Nat. Phys.* **14**, 621–628 (2018).
46. A. Pathak, S. Kumar, Independent regulation of tumor cell migration by matrix stiffness and confinement. *Proc. Natl. Acad. Sci. U. S. A.* **109**, 10334–10339 (2012).
47. M. R. Zanotelli, A. Rahman-Zaman, J. A. VanderBurgh, P. V. Taufalele, A. Jain, D. Erickson, F. Bordeleau, C. A. Reinhart-King, Energetic costs regulated by cell mechanics and confinement are predictive of migration path during decision-making. *Nat. Commun.* **10**, 1–12 (2019).
48. S. P. Carey, A. Rahman, C. M. Kraning-Rush, B. Romero, S. Somasegar, O. M. Torre, R. M. Williams, C. A. Reinhart-King, Comparative mechanisms of cancer cell migration through 3D matrix and physiological microtracks. *Am. J. Physiol. - Cell Physiol.* **308**, C436–C447 (2015).
49. P. Mistriotis, E. O. Wisniewski, K. Bera, J. Keys, Y. Li, S. Tuntithavornwat, R. A. Law, N. A. Perez-Gonzalez, E. Erdogmus, Y. Zhang, R. Zhao, S. X. Sun, P. Kalab, J. Lammerding, K. Konstantopoulos, Confinement hinders motility by inducing RhoA-mediated nuclear influx, volume expansion, and blebbing. *J. Cell Biol.* **218**, 4093–4111 (2019).
50. J. Li, D. J. Mooney, Designing hydrogels for controlled drug delivery. *Nat. Rev. Mater.* **1** (2016), doi:10.1038/natrevmats.2016.71.
51. L. Gu, D. J. Mooney, Biomaterials and emerging anticancer therapeutics: Engineering the microenvironment. *Nat. Rev. Cancer*. **16**, 56–66 (2016).
52. J. a. Rowley, G. Madlambayan, D. J. Mooney, Alginate hydrogels as synthetic extracellular matrix materials. *Biomaterials*. **20**, 45–53 (1999).

53. D. Schild, A. Jung, H. A. Schultens, Localization of calcium entry through calcium channels in olfactory receptor neurones using a laser scanning microscope and the calcium indicator dyes Fluo-3 and Fura-Red. *Cell Calcium*. **15**, 341–348 (1994).
54. P. Walczysko, E. Wagner, J. T. P. Albrechtová, Use of co-loaded Fluo-3 and Fura Red fluorescent indicators for studying the cytosolic Ca2+ concentrations distribution in living plant tissue. *Cell Calcium*. **28**, 23–32 (2000).
55. O. Iamshanova, P. Mariot, V. Lehen'kyi, N. Prevarskaya, Comparison of fluorescence probes for intracellular sodium imaging in prostate cancer cell lines. *Eur. Biophys. J.* **45**, 765–777 (2016).
56. C. L. Gilchrist, H. A. Leddy, L. Kaye, N. D. Case, K. E. Rothenberg, D. Little, W. Liedtke, B. D. Hoffman, F. Guilak, TRPV4-mediated calcium signaling in mesenchymal stem cells regulates aligned collagen matrix formation and vinculin tension. *Proc. Natl. Acad. Sci. U. S. A.* **116**, 1992–1997 (2019).
57. M. K. Kim, D. S. Min, Y. J. Park, J. H. Kim, S. H. Ryu, Y. S. Bae, Expression and functional role of formyl peptide receptor in human bone marrow-derived mesenchymal stem cells. *FEBS Lett.* **581**, 1917–1922 (2007).
58. M. B. Jones, G. R. Fulford, C. P. Please, D. L. S. McElwain, M. J. Collins, Elastohydrodynamics of the eyelid wiper. *Bull. Math. Biol.* **70**, 323–343 (2008).
59. G. Salbreux, J. F. Joanny, J. Prost, P. Pullarkat, Shape oscillations of non-adhering fibroblast cells. *Phys. Biol.* **4**, 268–284 (2007).
60. H. Jiang, S. X. Sun, Cellular pressure and volume regulation and implications for cell mechanics. *Biophys. J.* **105**, 609–619 (2013).

Acknowledgments

We would like to thank all members of the Chaudhuri lab for helpful discussion and Marc Levenston (Stanford University) for use of equipment. We also thank the Stanford Cell Sciences Imaging Facility for Imaris software access. H.L. acknowledges financial support from the Stanford Bio-X fellowship.

Funding

This work was supported by funding from the National Science Foundation for O.C. (CMMI 1846367). Computational work was supported by NCI Awards (U01CA202177, U54CA193417, and R01CA232256), NIBIB Award (R01EB017753) and the NSF Center for Engineering Mechanobiology (CMMI-154857).

Author contributions

H. Lee and O. Chaudhuri designed the experiments. H. Lee performed experiments, data analysis, and statistical tests. K. Adebawale generated representative 3D cell track reconstructions for cells. J. Chang performed western blots to confirm the knocking down proteins by siRNA treatments. F. Alisafaei, and V. B. Shenoy. performed computer simulations and analysis. H. Lee, F. Alisafaei, V. B. Shenoy, and O. Chaudhuri wrote the manuscript.

Competing interests

All authors declare no competing interests.

Data and materials availability

Data, materials, and custom-made scripts of code for the main text or the supplementary materials are available from the corresponding author upon reasonable request.

Supplementary Materials:

Supplementary Text

Figures S1-S11

Movies S1-S5

Figures

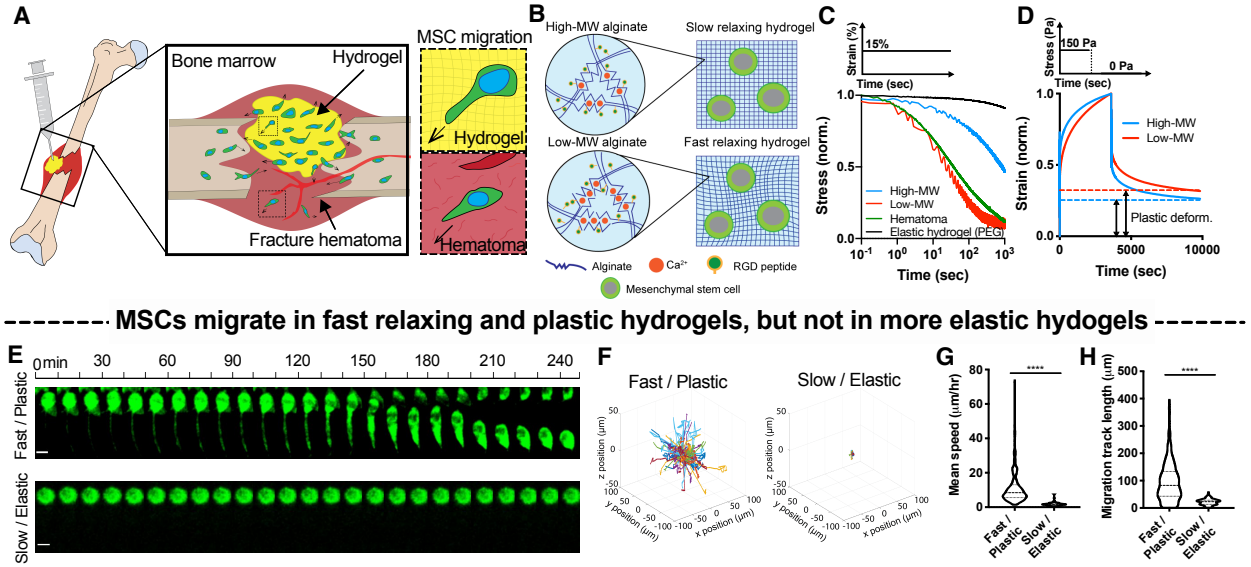

Fig. 1. Mesenchymal stem cells (MSCs) migrate in confining viscoelastic matrices, but not in more elastic matrices. (A) Schematics of MSC migration in a fracture hematoma and in transplanted hydrogels applied for MSCs delivery for bone regeneration. **(B)** Schematics of alginate hydrogels composed of different molecular weights of alginate. **(C)** Representative stress relaxation profiles of hydrogels with fast and slow stress relaxation. The relaxation profiles of a covalently crosslinked PEG hydrogel and a human fracture hematoma(*5*) are shown for comparison. **(D)** Representative plasticity test profiles of hydrogels with fast and slow stress relaxation. **(E)** Representative time-lapse image of MSC migration over time in fast relaxing hydrogel (Fast) and in slow relaxing hydrogel (Slow), respectively. Maximum intensity projections of R18 cell membrane dye signal are shown. **(F)** Representative 3D track reconstructions for cell migration in fast relaxing hydrogels and slow relaxing hydrogels. Grid size = 10 μm. **(G)** Mean speeds for migrating cells in fast and slow relaxing hydrogels. (n > 200 single cells) **(H)** Track length of migrating cells in each hydrogels. (n > 200 single cells) **** $p<0.0001$ by Student's t-test. All scale bars = 10 μm. All data are shown as mean ± s.e.m.

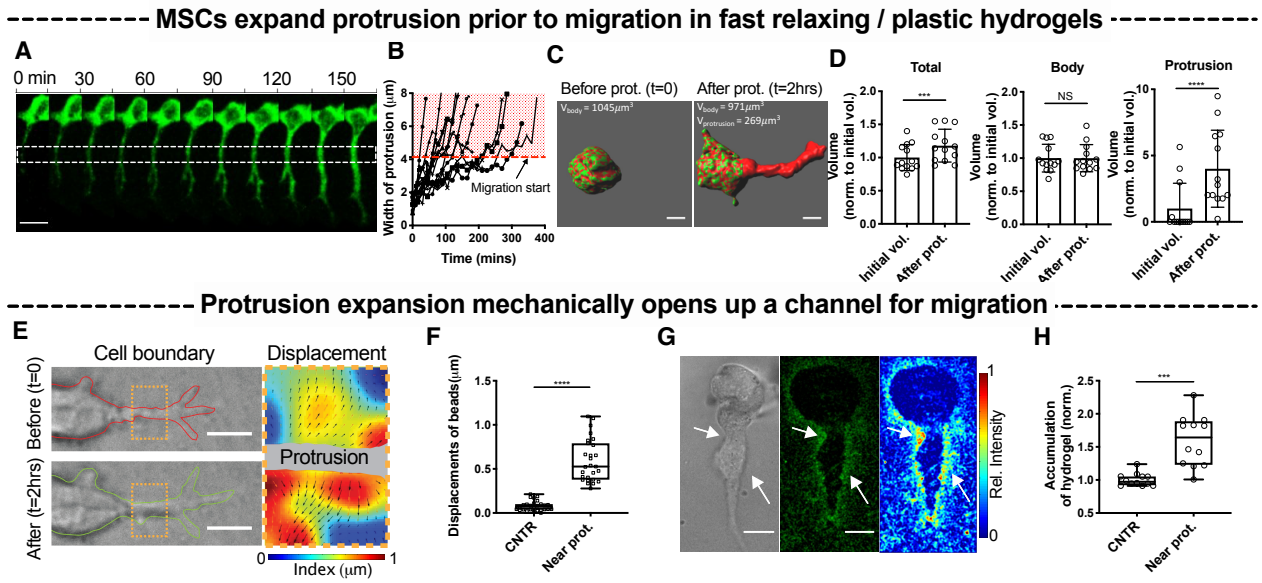

Fig. 2. MSCs physically open up a migration path through expansion of protrusions. (A) Representative time lapse images of cells migrating. Widening protrusions are shown in white dotted box. **(B)** Tracings of protrusion widths for migrating cells. (n > 20). Red dotted line indicates the average width of protrusion when cells start to migrate in the direction of the protrusion. **(C)** Representative 3D renderings of a single cell before and after protruding. **(D)** Quantification of altered total volume, altered volume of body part and altered volume of protrusion part before (t = 0) and after cell protrusion (n > 10 single cells). **(E)** Bead displacements obtained from a single z-plane before and after widening protrusion were used to model the matrix displacement field illustrating a heat map with displacement magnitudes and directions. **(F)** Maximum bead displacements via cell protrusion around cells. (n > 30 beads) **(G)** Densification of fluorescein-conjugated alginate around protrusions. **(H)** Densified matrix were quantified as intensity and compared with control. (n = 15 images) *** $p<0.001$ and **** $p<0.0001$ by Student's t-test. All experiments in figure are from fast relaxing hydrogels. All scale bars = 10 μm. All data are shown as mean ± s.e.m.

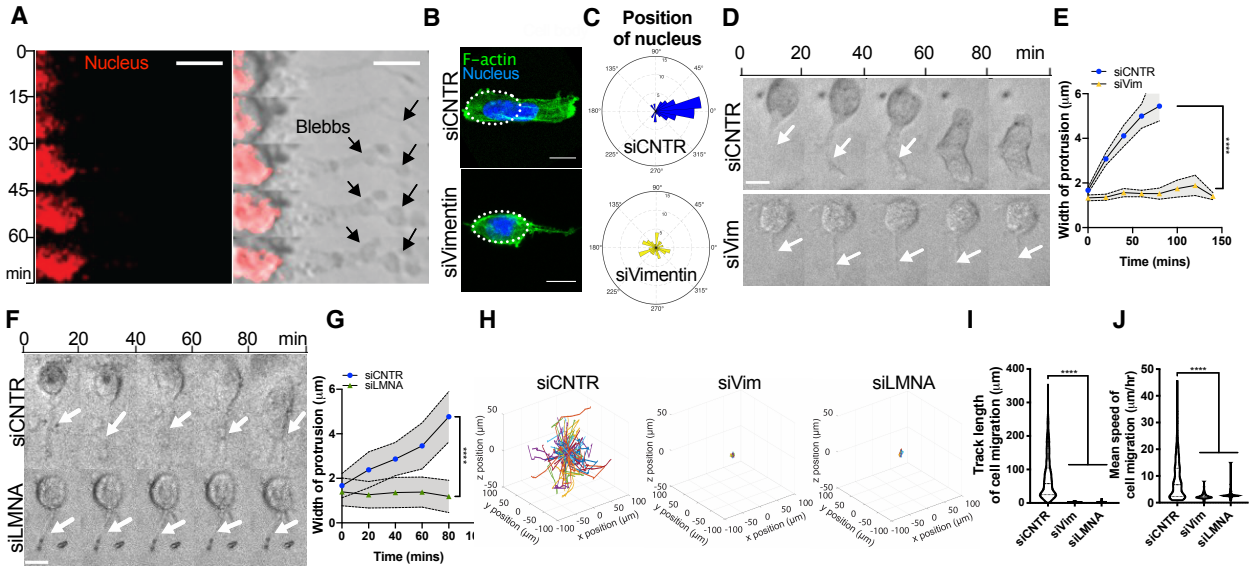

Fig. 3. A nuclear piston mediated by vimentin and lamins induces protrusion expansion. (A) Representative time lapse images of the nucleus in a cell as protrusion expands. Blebs indicated by black arrows. **(B)** Representative images of a protruding MSC transfected with control (siCNTR) or vimentin (siVimentin) siRNA. Area of cell body is indicated by white dotted line. **(C)** Polar distribution of relative location of nucleus in cell body (n > 50 single cells) **(D)** Representative time lapse images of protruding MSCs. The protrusions are indicated by white arrows. **(E)** Tracings of protrusion width for a protruding MSC. (n > 15 single cells) **(F)** Representative time lapse images (bright field images) of a protruding MSC transfected with control or lamin (siLMNA) siRNA. The protrusion of cell is indicated by white arrows. **(G)** Tracings of protrusion widths for a protruding MSC. (n > 15 single cells) **** p<0.0001 by student t-test. **(H-J)** Representative 3D track reconstructions **(H)**, track lengths **(I)**, and mean speeds **(J)** for migration of MSCs. (n > 200 single cells)**.** All Scale bars, 10 μm. *** p<0.001 and ****p<0.0001 by student t-test and by one-way ANOVA test for I and J. All data are shown as mean ± s.e.m.

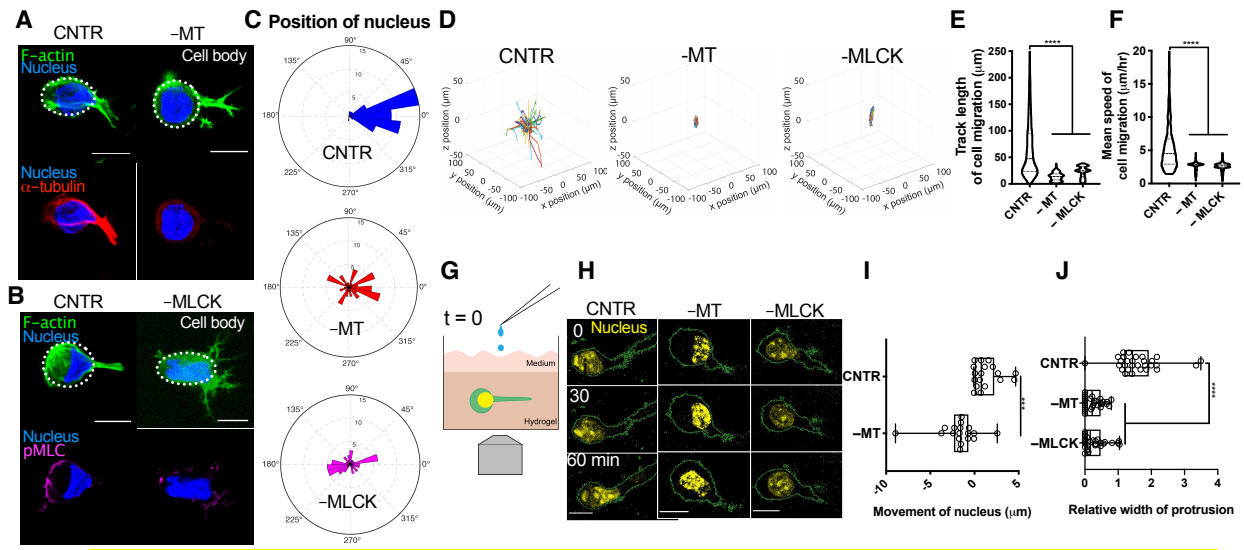

Fig. 4. Nuclear piston movements are mediated by microtubules and myosin contractions.
(A-B) Representative immunofluorescence images for F-actin, α-tubulin, phospho-myosin light chain (pMLC), and nucleus of a protruding MSC with treatment of Nocodazole (-MT), ML-7 (-MLCK) or vehicle-alone control (CNTR). **(C)** Polar distribution of relative location of cell nucleus in cell body of MSCs. (n > 50 single cells) **(D)** Representative 3D track reconstructions for migration of MSC. **(E)** Track length of migrating cells treated with each inhibitors or vehicle-alone control. (n > 200 single cells) **(F)** Mean speeds for migrating cells treated with each inhibitors or vehicle-alone control. (n > 200 single cells) **(G)** Schematic of inhibition test. After finding a protruding cell with the nucleus located at the base of protrusion, inhibitors are delivered and the movement of cell nucleus is monitored. **(H)** Representative time lapse images showing nuclear movements over time in cell body. **(I-J)** Quantification of nuclear movements (I) and of relative width of protrusion (J) after 1 hour of treatment (n > 15 single cells). All Scale bars, 10 μm. *** $p<0.001$ and **** $p<0.0001$ by student t-test and by one-way ANOVA test respectively. All data are shown as mean ± s.e.m.

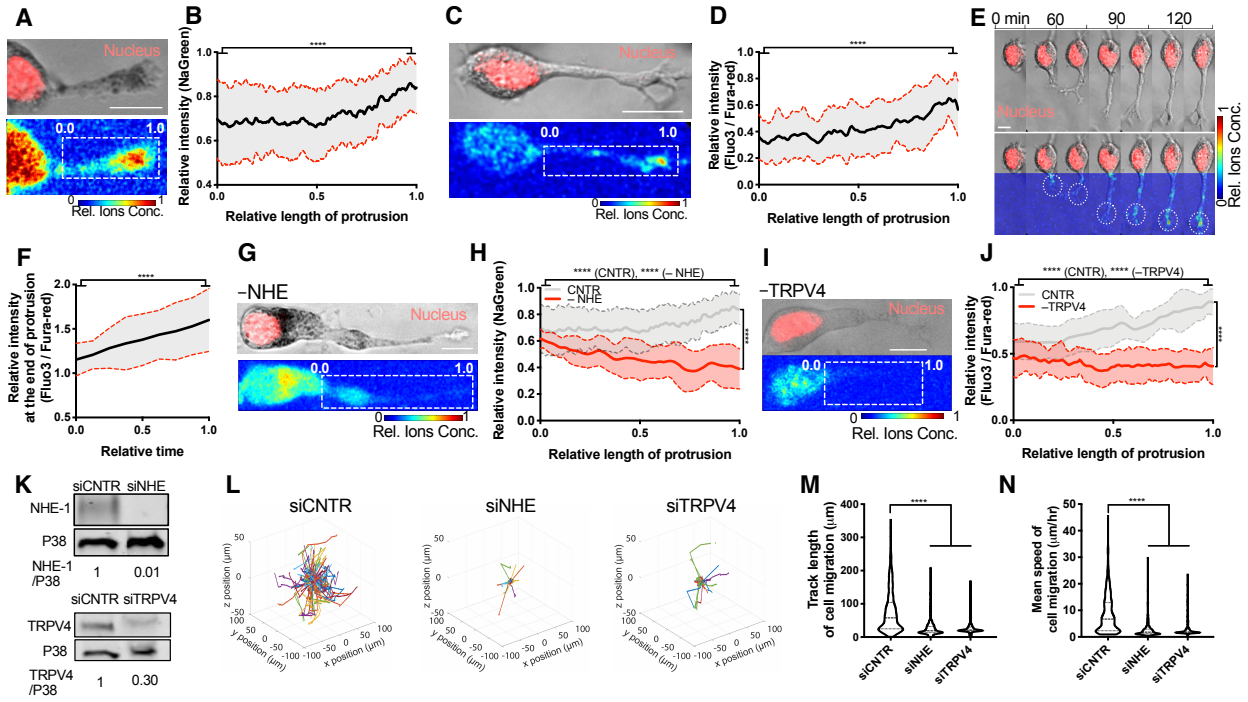

Fig. 5. Ion influx at protrusion mediated by NHE and TRPV4 ion channels. (A) Intracellular sodium ion imaging in cell protrusion (white dotted box). **(B)** Distribution profile of intracellular sodium ions along protrusion. (n>45 single cells) **(C)** Intracellular calcium ion imaging in cell protrusion (white dotted box). **(D)** Distribution profile of intracellular calcium ions along protrusion. (n>45 single cells) **(E)** Time-lapse images of a cell merged with heatmaps of calcium ion concentration. Scale bar, 5 μm. **(F)** Evolution intracellular calcium ion concentration at end of protrusion. (n>45 single cells) **(G-H)** Representative images and profiles of intracellular sodium ions with NHE inhibition. (n>45 single cells). **(I-J)** Representative images and profiles of intracellular calcium ions with TRPV4 inhibition. (n>45 single cells). **(K)** Western blot analysis of NHE-1 and TRPV4 protein expression in MSCs with siRNA of NHE-1 (siNHE), TRPV4 (siTRPV4), or control (siCNTR) . **(L–N)** Representative 3D track reconstructions **(L)**, track lengths**(M)**, and mean speeds **(N)** for migration of MSCs. (n>200 single cells) Scale bars are 10 μm unless otherwise indicated. *** p<0.001 and **** p<0.0001 by one-way ANOVA test. All data are shown as mean ± s.e.m, including profile graphs.

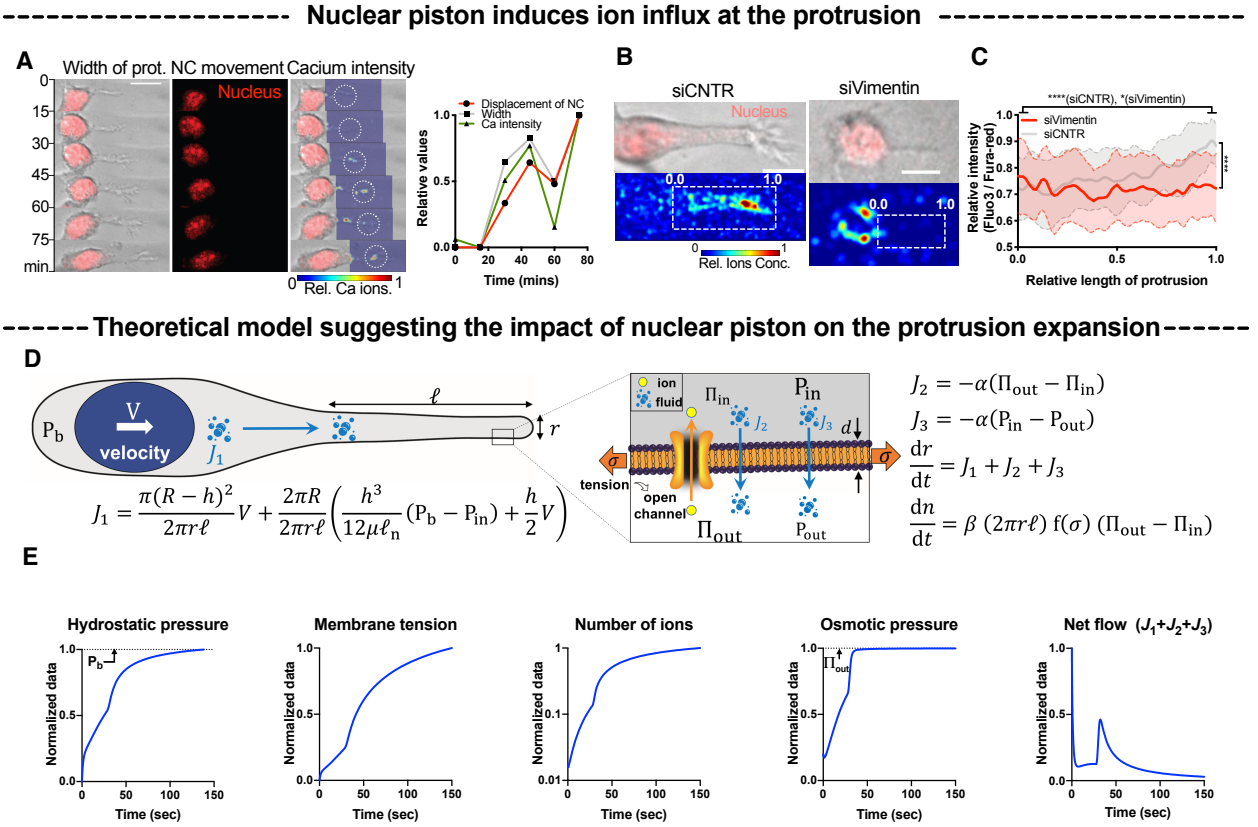

$$J_1 = \frac{\pi(R-h)^2}{2\pi r\ell}V + \frac{2\pi R}{2\pi r\ell}\left(\frac{h^3}{12\mu\ell_n}(P_b - P_{in}) + \frac{h}{2}V\right)$$

$$J_2 = -\alpha(\Pi_{out} - \Pi_{in})$$

$$J_3 = -\alpha(P_{in} - P_{out})$$

$$\frac{dr}{dt} = J_1 + J_2 + J_3$$

$$\frac{dn}{dt} = \beta\,(2\pi r\ell)\,f(\sigma)\,(\Pi_{out} - \Pi_{in})$$

Fig. 6. Theoretical model and experiments suggest that nuclear piston activates ion channels, which allow an influx of ions into the protrusion. (A) Representative time lapse images of nuclear movements and calcium ions at the tip of the protrusion in one cell over a 80 min timeframe. Heat maps for relative calcium ion concentration at the protrusion are shown merged with bright field images. Scale bar, 10 μm. Graph on the right shows the change in protrusion width, nuclear displacement, and the concentration of intracellular calcium ions of the cell shown on the left. **(B-C)** Representative images and profiles of intracellular calcium ions in the protrusion of MSCs transfected with vimentin siRNA or control siRNA. . (n > 45 single cells) **(D)** Schematics and equations for the theoretical model of the nuclear piston and protrusion expansion. **(E)** Theoretical model predictions of hydrostatic pressure, membrane tension, the number of intracellular ion, osmotic pressure, and net flow of fluid in the protrusion over time when nucleus move toward protrusion. Scale bar, 10 μm. Heat maps indicates relative calcium ion concentration. *** $p<0.001$ and **** $p<0.0001$ by one-way ANOVA test. All data are shown as mean ± s.e.m. In profile graphs, mean and s.e.m are indicated by solid lines and dotted lines, respectively.

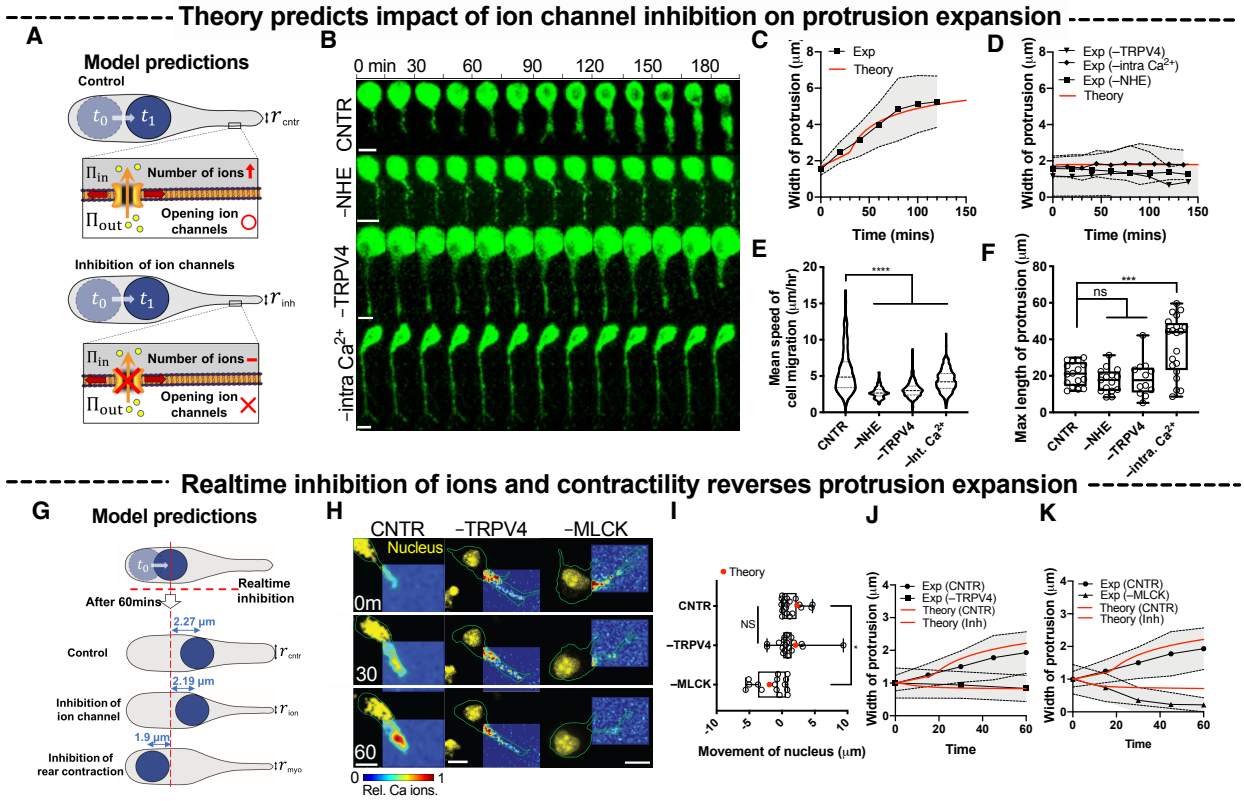

Fig. 7. Theoretical model and experiments show that influx of ions into protrusion increases osmotic pressure sufficiently to outcompete hydrostatic pressure and expand protrusions. (A) Schematic of ion channel inhibition in model. **(B)** Representative time lapse images of protruding cells in the presence of the indicated inhibitor. **(C-D)** Comparison of theoretical results to experimental measurements of protrusion widths in the presence of vehicle-alone control (C) or each inhibitor (D). **(E)** Mean speeds of migrating cells in the presence of each inhibitors or vehicle-alone control. (n>230) **(F)** Maximum length of protrusions with each inhibitor or the vehicle-alone control. **(G)** Schematic of real-time inhibition of ion channels or actomyosin contractility in model. **(H)** Representative time-lapse images of nucleus and calcium ion concentrations in MSC with treatment of each inhibitor or vehicle-alone control. Scale bar, 10 μm. **(I)** Comparison of theoretical results to experimental measurements after 1 hour of treatment. (n>15) **(J-K)** Theoretical and experimental tracings of protrusion widths for a protruding MSC with treatment of TRPV4 inhibitor (J), MLCK inhibitor (K), or vehicle-alone control. (n>25) * p<0.05, *** p<0.001, and **** p<0.0001 by one-way ANOVA test. All data are shown as mean ± s.e.m, including in tracing graphs.

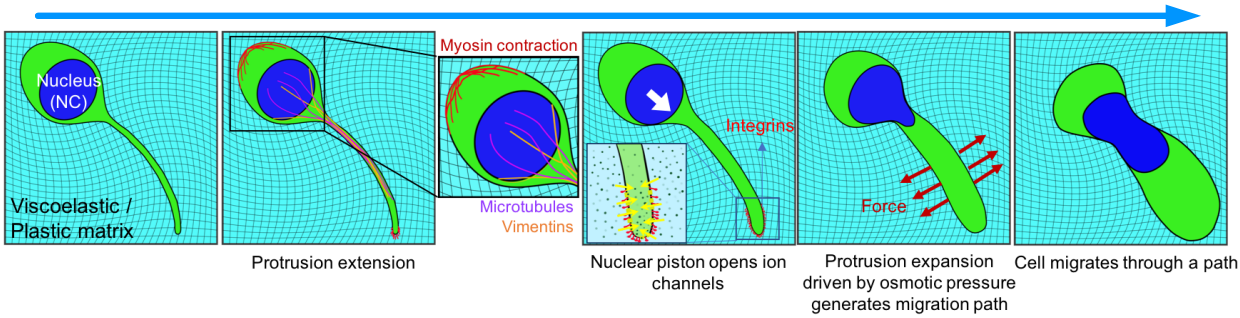

Fig. 8. The nuclear piston generates migration paths in viscoelastic and plastic matrices. Schematic of proposed mechanism explaining how MSCs generate a migration path in viscoelastic matrix using the nuclear piston.

Title: The nuclear piston activates mechanosensitive ion channels to generate cell migration paths in confining microenvironments

Authors: Hong-pyo Lee[1], Farid Alisafaei[2], Kolade Adebawale[3], Julie Chang[4], Vivek B. Shenoy[2], Ovijit Chaudhuri[1*]

*Correspondence to: chaudhuri@stanford.edu.

This PDF file includes:

Supplementary Text
Figure. S1 to S11
Captions for Movies S1 to S5

Other Supplementary Materials for this manuscript include the following:

Movies S1 to S5

Supplementary Text

Theoretical model description

Here, we propose a theoretical model to explain the mechanism through which the actomyosin-based movement of the nucleus regulates the protrusion expansion and the transport of fluid and ions. To describe this mechanism, consider the movement of the nucleus in fig. S11A. With the forward movement of the nucleus, the fluid in front of the nucleus is pushed into the protrusion and expands the protrusion where the rate of expansion can be determined as follows

$$\frac{\mathrm{d}r}{\mathrm{d}t} = \frac{\pi R^2}{2\pi r \ell} V \tag{1}$$

where r is the protrusion radius, R is the radius of the cell body, ℓ is the length of the protrusion, and V is the velocity of the nucleus which can be estimated from our experiments or can be calculated as an unknown variable in equation (11). Note that the radius of the nucleus in equation (1) is assumed to be equal to the radius of the cell body. However, we can extend the model by assuming a small gap h between the nucleus and the cell body (fig. S11A). Using the lubrication theory(*15*), we then relate the fluid pressure P to the fluid velocity u in the gap

$$\frac{\partial \mathrm{P}}{\partial x} = \mu \frac{\partial^2 u}{\partial y^2} \tag{2}$$

where μ is the fluid viscosity. Applying no-slip boundary conditions ($u = V$ at $y = 0$, and $u = 0$ at $y = h$), we have

$$u = \frac{1}{2\mu}\frac{\partial \mathrm{P}}{\partial x} y(y-h) - V\left(\frac{y}{h} - 1\right) \tag{3}$$

Using equation (3), we can determine the volume flux through the gap

$$Q = 2\pi R \int_0^h u \,\mathrm{d}y = 2\pi R\left(-\frac{h^3}{12\mu}\frac{\partial \mathrm{P}}{\partial x} + \frac{h}{2}V\right) = 2\pi R\left(\frac{h^3}{12\mu \ell_{\mathrm{n}}}(\mathrm{P_b} - \mathrm{P_{in}}) + \frac{h}{2}V\right) \tag{4}$$

where ℓ_{n} is the length of the nucleus, $\mathrm{P_b}$ is the hydrostatic pressure in the cell posterior generated by the actomyosin contractility, and $\mathrm{P_{in}}$ is the hydrostatic pressure in the protrusion. With Q at hand, we can revise equation (1) as follows

$$\frac{\mathrm{d}r}{\mathrm{d}t} = \frac{\pi(R-h)^2}{2\pi r \ell} V + \frac{2\pi R}{2\pi r \ell}\left(\frac{h^3}{12\mu \ell_{\mathrm{n}}}(\mathrm{P_b} - \mathrm{P_{in}}) + \frac{h}{2}V\right) \tag{5}$$

where the sum of the two terms on the right-hand side of the equation is represented by J_1 in Fig. 4A. In addition to J_1, the efflux and influx of the fluid through the membrane can also change the protrusion radius r. Therefore, we revise equation (5) to account for the fluid transport due to the osmotic and hydrostatic pressure gradients across the membrane as the fluid flows (i) from lower to higher osmotic pressure, and (ii) from higher to lower hydrostatic pressure(*16*, *17*)

$$\frac{\mathrm{d}r}{\mathrm{d}t} = \frac{\pi(R-h)^2}{2\pi r\ell}V + \frac{2\pi R}{2\pi r\ell}\left(\frac{h^3}{12\mu\ell_\mathrm{n}}(\mathrm{P_b}-\mathrm{P_{in}}) + \frac{h}{2}V\right) - \alpha(\Pi_{\mathrm{out}}-\Pi_{\mathrm{in}}) - \alpha(\mathrm{P_{in}}-\mathrm{P_{out}}) \quad (6)$$

where α represents the rate constant of fluid transport. The third term in equation (6) is represented by J_2 in Fig. 4A and denotes the fluid transport due to the difference between the osmotic pressures outside (Π_{out}) and inside (Π_{in}) of the protrusion. Similarly, the fourth term denotes the fluid transport due to the difference between the hydrostatic pressures inside ($\mathrm{P_{in}}$) and outside ($\mathrm{P_{out}}$) of the protrusion and is represented by J_3 in Fig. 4A. In addition to the fluid flux, ions can also flow in and out of the protrusion. As observed in our experiments, the flux of ions is regulated by mechanosensitive ion channels which are activated with stretching the membrane. With the opening of the mechanosensitive channels, ions can flow in and out of the protrusion in the direction of the ion concentration gradient across the membrane (Fig. 4A). Thus, the ion flux rate $\mathrm{d}n/\mathrm{d}t$ can be calculated as a function of the difference between the osmotic pressures outside (Π_{out}) and inside (Π_{in}) of the protrusion(*17*)

$$\frac{\mathrm{d}n}{\mathrm{d}t} = \beta\ (2\pi r\ell)\ \mathrm{f}(\sigma)\ (\Pi_{\mathrm{out}} - \Pi_{\mathrm{in}}) \quad (7)$$

where β is the rate constant of ion transport, $2\pi r\ell$ is the surface area of the protrusion and $\mathrm{f}(\sigma)$ represents the opening of the channel as a function of the membrane tension σ (fig. S11b). The membrane tension can be related to the protrusion radius r using the following constitutive equation

$$\sigma = \frac{E(r-r_0)}{r_0} \quad (8)$$

where r_0 is the initial radius of the protrusion, and E is the elastic modulus of the membrane/cortex. With σ at hand as a function of r, the hydrostatic pressures inside the protrusion ($\mathrm{P_{in}}$) can be also determined from the following equation using the force balance in the circumferential direction of the cylindrical protrusion

$$\mathrm{P_{in}} = \mathrm{P_{out}} + \frac{d}{r}\sigma \quad (9)$$

where d is the thickness of the membrane/cortex (Fig. 4a). The osmotic pressure inside the protrusion can be expressed in terms of the protrusion radius r and the number of ions n

$$\Pi_{\text{in}} = \frac{nRT}{\pi r^2 \ell} \qquad (10)$$

where $\pi r^2 \ell$ is the protrusion volume, T is the absolute temperature, and R is the gas constant. Finally, the velocity of the nucleus V can be obtained from the force balance on the nucleus

$$\pi(R-h)^2 \, \mathrm{P_b} - \pi (R-h)^2 \, \mathrm{P_{in}} - 2\pi(R-h)\ell_{\mathrm{n}} \, \mu_{\mathrm{n}} \, V = 0 \qquad (11)$$

where the first, second, and third terms are the force on the back of the nucleus, the force on the front of the nucleus, and the shear force on the lateral surface of the nucleus, respectively. In equation (11), μ_{n} is the friction coefficient which can be assumed to be inversely proportional to the protrusion radius r as smaller protrusions generate higher resistance forces against nuclear movement. The two unknown variables r and n can be obtained by solving the two coupled equations (6) and (7) where σ, $\mathrm{P_{in}}$, Π_{in}, and V can be expressed in terms of r and n from equations (8-11). Equations (6) and (7) need two initial conditions; r_0 and n_0 which are the initial radius of the protrusion and the initial number of ions, respectively. The initial radius of the protrusion is 0.75 μm ($r = r_0$ at $t = 0$) which is estimated from our experiments. fig. S8 shows the model prediction for two different n_0; (i) low initial number of ions ($\Pi_{\mathrm{in}} < \Pi_{\mathrm{out}}$ at $t = 0$), and (ii) high initial number of ions ($\Pi_{\mathrm{in}} > \Pi_{\mathrm{out}}$ at $t = 0$). The model shows similar behavior for both cases which indicates that, independent of the initial number of ions n_0, cell protrusions cannot expand in the absence of protrusion ion channels.

Supplementary Figures

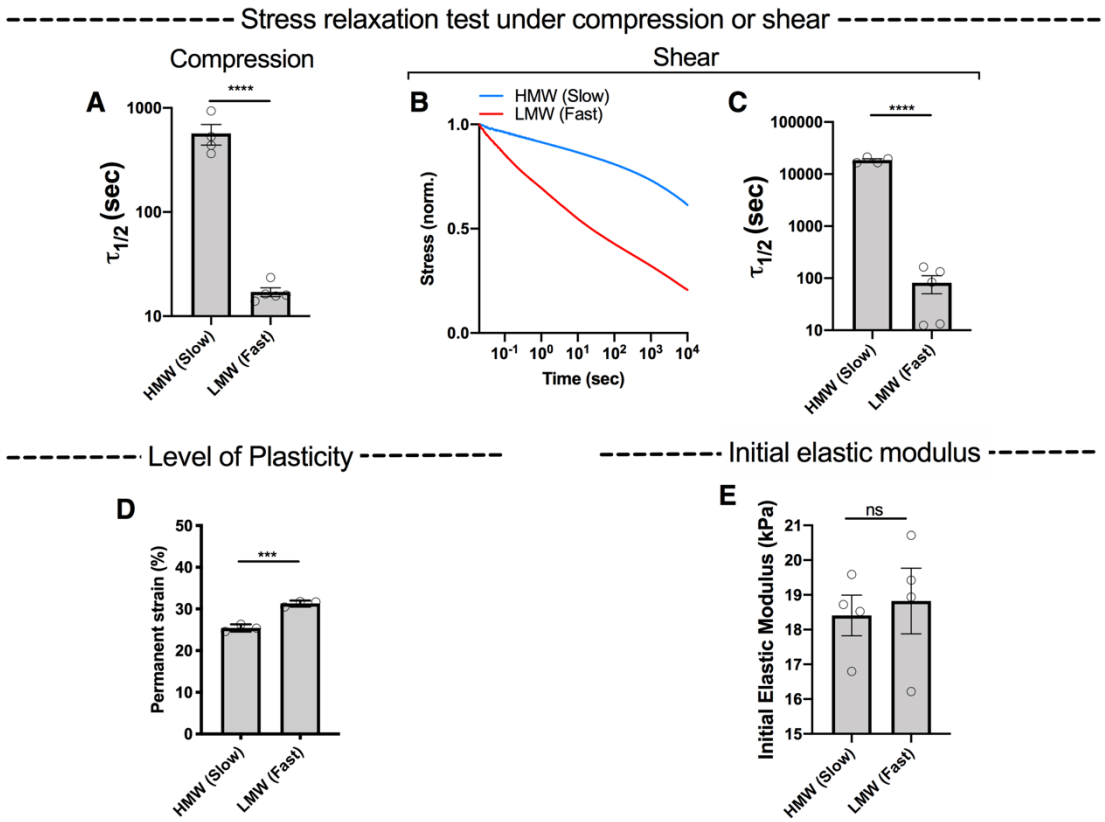

Fig. S1. Mechanical properties of alginate hydrogels. (A) Quantification of the time scale of stress relaxation, $\tau_{1/2}$, for the different alginate hydrogels under compression. **(B)** Normalized stress relaxation profiles of alginate gels under shear. **(C)** Quantification of the time scale of stress relaxation, $\tau_{1/2}$ under shear. **(D)** Quantification of percentage of permanent strain (plasticity) of different alginate hydrogels from creep and recovery tests. **(E)** Initial elastic modulus of the different alginate hydrogels. *** $p < 0.001$ and **** $p < 0.0001$ indicate a statistically significant difference when compared to high MW alginate (HMW) condition by Student t-test. All data are shown as mean ± s.e.m, $n \geq 4$ replicates per conditions.

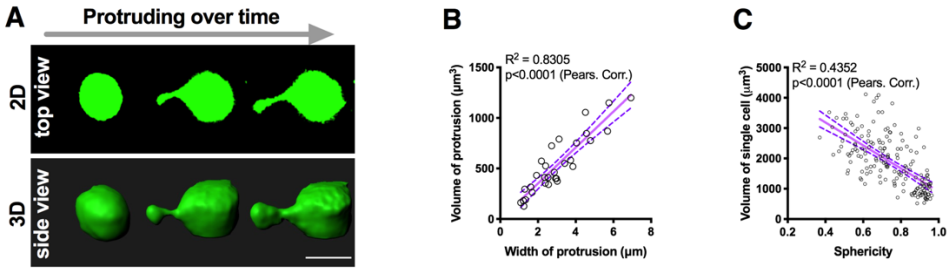

Fig. S2. Protrusion extension and widening are accompanied by volume expansion of protrusion. (A) Top 2D view and side 3D reconstructing view of representative images of a protruding cell over time. **(B)** Scatter plots of the volume versus the width of cell protrusions. (n = 30 single cells) Linear regression analysis indicated a linear correlation between cell volume of protrusion and width of protrusion. **(C)** Scatter plot of cell volume versus sphericity of cells cultured in fast relaxing hydrogels. (n = 175 single cells)

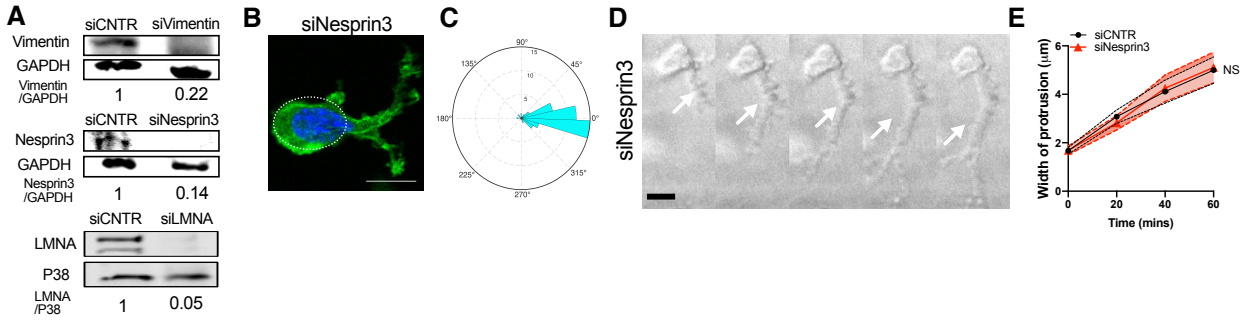

Fig. S3. Nuclear piston and protrusion expansion are not mediated by nesprin3. (A) Western blot analysis of vimentin and nesprin3 protein expression in MSCs transfected with vimentin siRNA, nesprin3 siRNA, lamin A/C siRNA, or control siRNA for 72 hrs. **(B)** Representative immunofluorescent images of a protruding MSC transfected with nesprin3 siRNA. Dotted line indicates the area of cell body. Scale bar, 10 μm. **(C)** Polar distribution of relative location of cell nucleus in cell body of MSCs, transfected with nesprin3 siRNA. **(D)** Representative time lapse images (bright field images) of a protruding MSC transfected with nesprin3 siRNA. The protrusion of cell is indicated by white arrows. Scale bar, 10 μm. **(E)** Tracings of protrusion widths for a protruding MSC transfected with nesprin3 siRNA or control siRNA. (n > 15 single cells) p-value > 0.05 is indicated as NS.

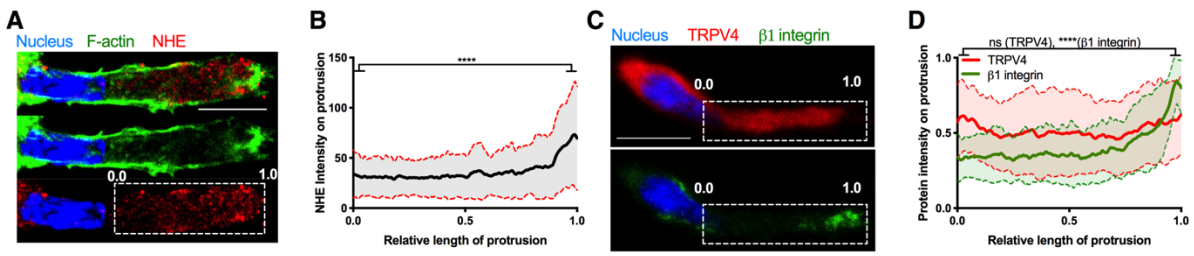

Fig. S4. Sodium-hydrogen exchange 1 (NHE), β1 integrins but not TRPV4 calcium ion channels exhibit higher densities at tip of protrusion. (A-B) Representative images (A) and profiles (B) of NHE along the protrusion of MSCs (white dotted box). **(C-D)** Representative images (C) and profiles (D) of TRPV4 calcium ion channels and β1 integrins along the protrusion of MSCs (white dotted box). Scale bar is 10 μm. n > 40 single cells. ns, p =0.3402 and **** p<0.0001 by student t-test. In profile graphs, mean and s.e.m are indicated by solid lines and dotted lines, respectively**.**

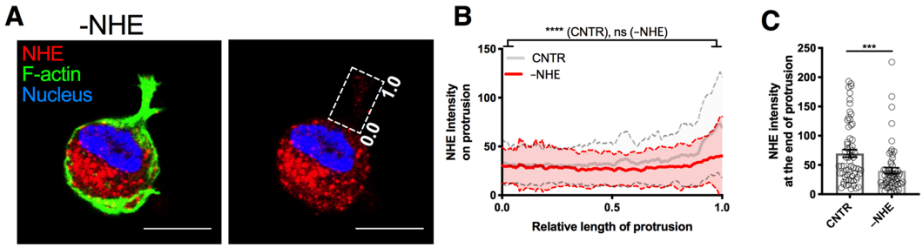

Fig. S5. Distribution of NHE ion channels along the protrusion of cells in the presence of NHE inhibitor (EIPA). (A-B) Representative images (A) and profiles (B) of distribution for NHE sodium ion channels along the protrusion of MSCs in the presence of NHE inhibitor (EIPA) or vehicle-alone control. Scale bar, 10 μm. **(C)** Quantification of intensity of NHE proteins at the end of protrusion with the treatment of NHE inhibitor (EIPA) or vehicle-alone control. ns, ***, and **** respectively indicate $p = 0.8647$, $p < 0.001$, and $p < 0.0001$ by student t-test. Data are shown as mean ± s.e.m. In profile graphs, mean and s.e.m are indicated by solid lines and dotted lines, respectively**.**

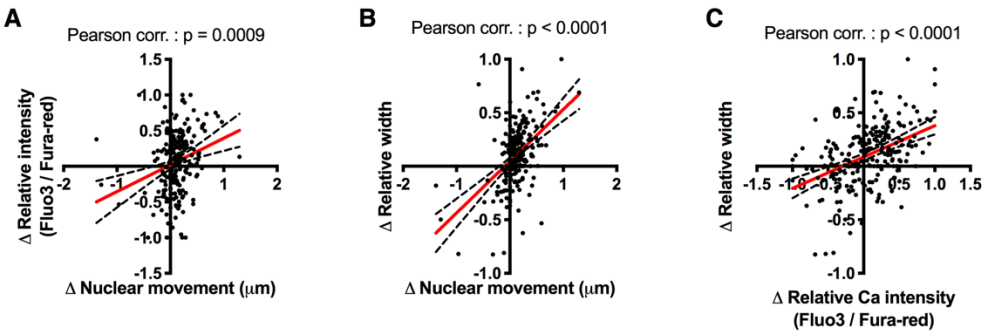

Fig. S6. Correlation between nucleus movements, altered width of protrusion, and accumulated calcium ion at the end of protrusion. (A-C) Based on image analysis with time lapse images, nucleus movements, altered width of protrusion, and accumulated calcium ions are shown as correlation plots. Red lines, regression lines. Dotted bands, 95% confidence intervals. Pearson corr indicates Pearson correlation coefficients.

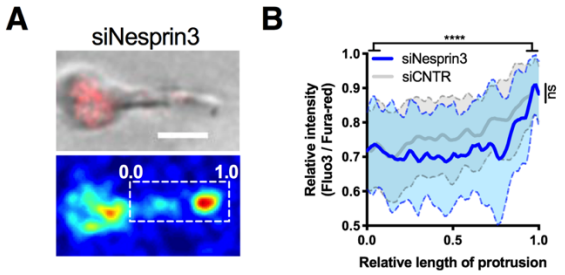

Fig. S7. Knockdown of nesprin3 does not impact higher concentrations of calcium ions at the tip of protrusion. (A-B) Representative images (A) and profiles (B) of intracellular calcium ions in the protrusion of MSCs transfected with Nesprin3 siRNA. Scale bar, 10 µm. n > 20 single cells. Heat map exhibits relative calcium ion concentration in the protrusion (white dotted box). ns indicates $p > 0.05$.

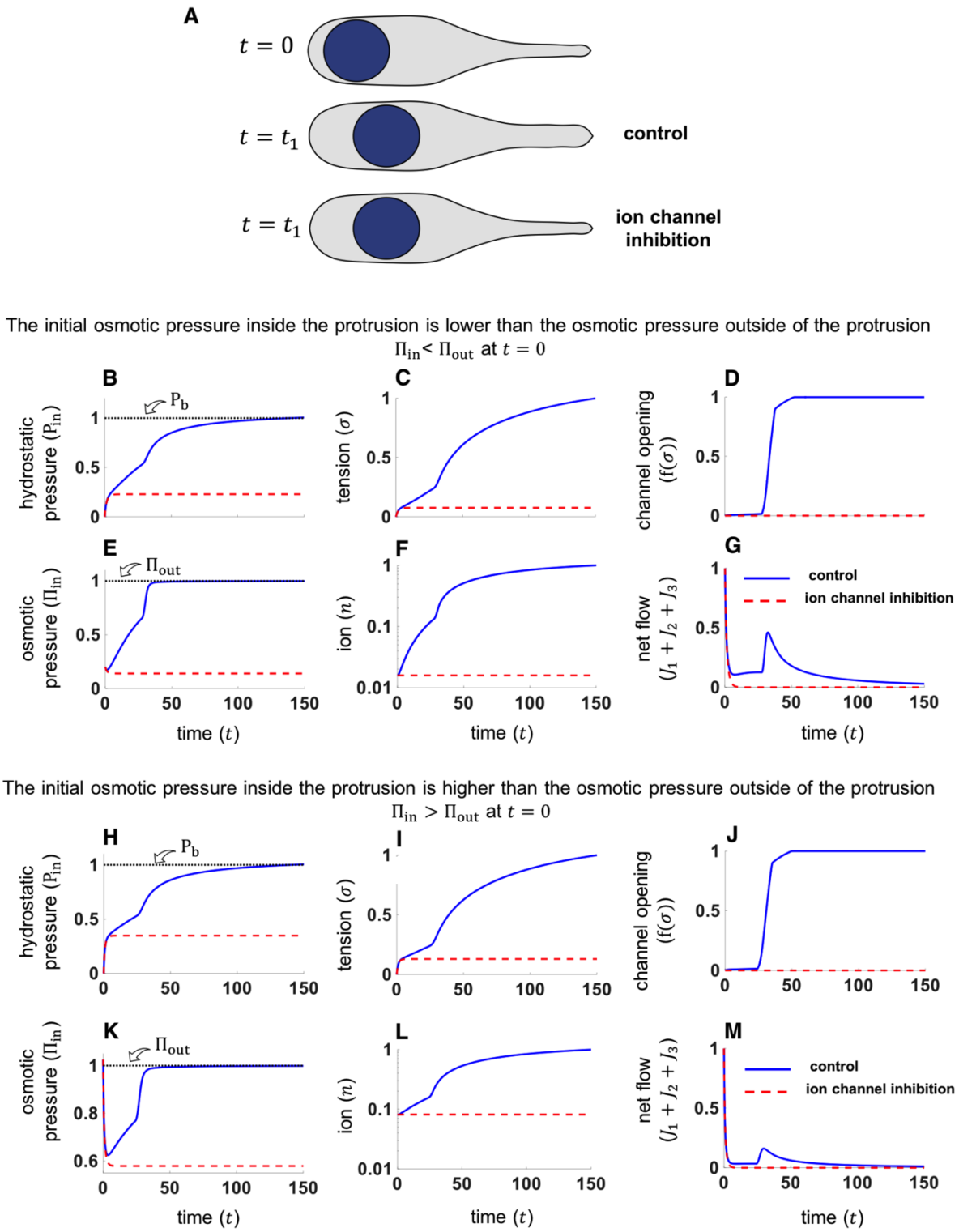

Fig. S8. Theoretical model shows the function of ion channels during protrusion expansion. **(A)** Schematics of simulating ion channels inhibition with theoretical model. **(B-M)** Theoretical model predictions of hydrostatic pressure (B, H), surface tension at the cell membrane (C, I), activated ion channels (D, J), osmotic pressure (E, K), the number of intracellular ions (F, L), and net flow of fluid (G, M) in the protrusion over time when ion channels are inhibited (red dotted line).

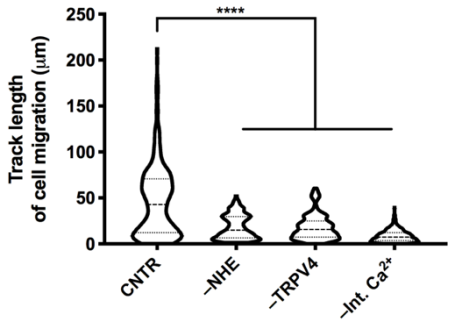

Fig. S9. The impact of NHE function, TRPV4 function, and intra cellular calcium ions on cell migration in hydrogels. Track length of migrating cells in the presence of each inhibitors or vehicle-alone control. ****p<0.0001 by one-way ANOVA test. n > 230 single cells. All data are shown as mean ± s.e.m

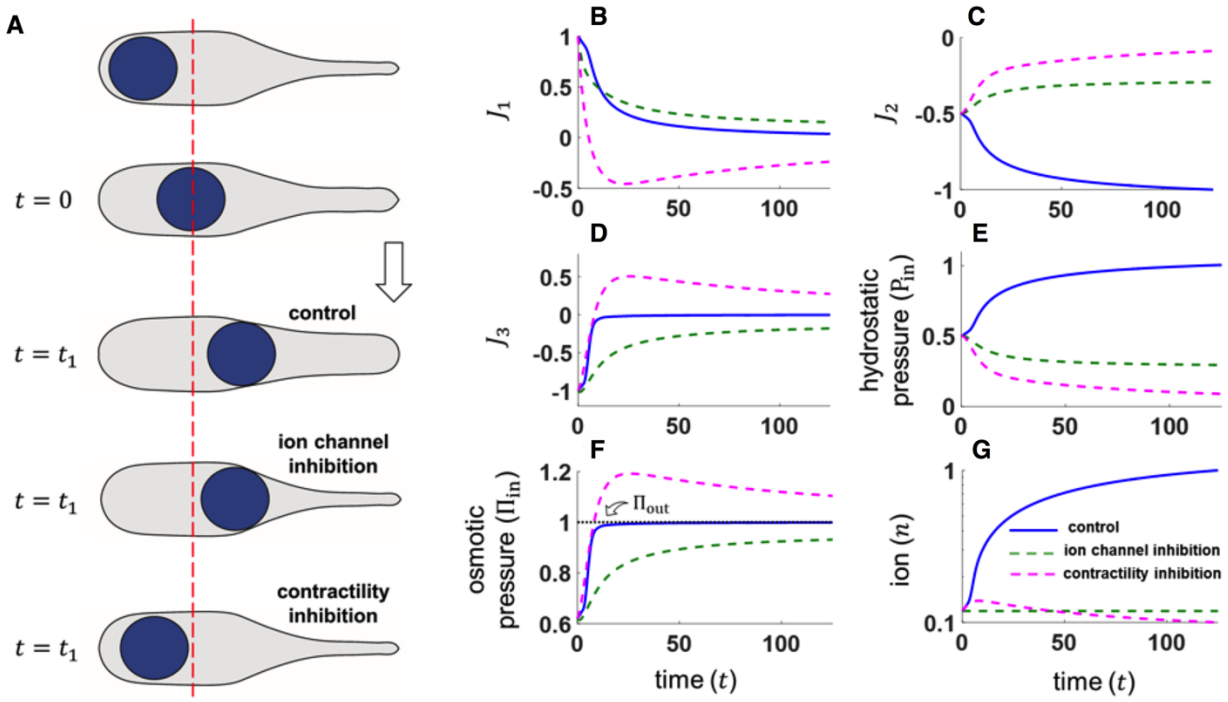

Fig. S10. Theoretical model predictions of altered nuclear location and protrusion expansion via real-time inhibitions of mechanosensitive ion channels or actomyosin contractility. (A) Schematics of model predictions. **(B-D)** Normalized fluid flux due to the nuclear movement (b), the hydrostatic pressure difference across the membrane (B), and the osmotic pressure difference across the membrane (D) where positive and negative values indicate influx and efflux of fluid, respectively. **(E-G)** Analytical model predictions of the normalized hydrostatic pressure (E), osmotic pressure (F), and number of ions (G) in the protrusion as functions of time (minute).

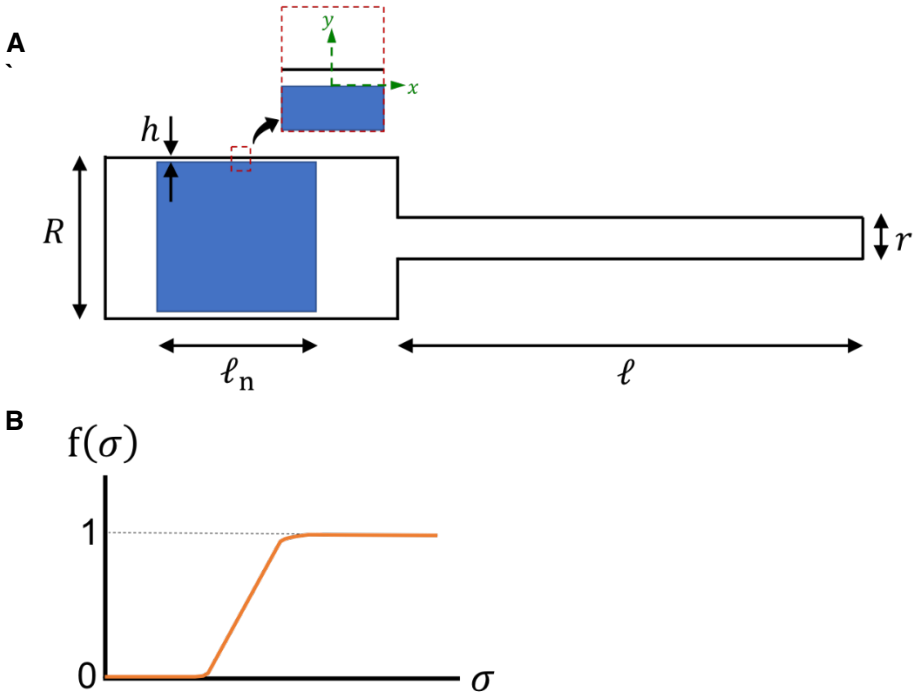

Fig. S11. Theoretical model of cells in which the movement of the nucleus regulates opening of ion channels and the protrusion expansion by the transport of fluid. (A) Schematics of the cell body which has a protrusion and a nucleus (blue rectangle). **(B)** Theoretical model of mechanosensitive ion channel activation by surface tension at the cell membrane.

Supplementary Movies

Movie S1. MSCs migrate in fast relaxing hydrogels. Cell membrane and nucleus are indicated by green and blue fluorescence, respectively. The surrounding matrix is indicated by red fluorescent microbeads embedded in hydrogels. Scale bar, 50 μm.

Movie S2. MSCs maintain rounded cell morphology and do not migrate in the slow relaxing hydrogels. Cell membrane and nucleus are indicated by green and blue fluorescence, respectively. For mapping the displacement of matrix, red fluorescent microbeads are embedded in hydrogels. Scale bar, 50 μm.

Movie S3. Protrusion expansion generates force to open the hole in hydrogels. Cell morphology and surrounding matrix are indicated by bright field image and red fluorescent beads. Red microbeads adjacent to the protrusion in yellow box are moved away from the protrusion when the protrusion is expanding. Scale bar, 10 μm.

Movie S4. Protrusion is expanded by movement of the nucleus towards and into the narrow entrance of the thin protrusions. Cell morphology and nucleus are indicated by bright field image and red fluorescence. Scale bar, 10 μm.

Movie S5. Blebs are observed at the cell membrane in protrusions following entry of the nucleus into the protrusion. Cell morphology and nucleus are indicated by bright field image and red fluorescence. Scale bar, 10 μm.